Towards magnetic force sensing of single molecules using suspended carbon nanotubes

by

Kyle Willick

A thesis
presented to the University of Waterloo
in fulfillment of the
thesis requirement for the degree of
Master of Science
in
Physics - Quantum Information

Waterloo, Ontario, Canada, 2014

Author's Declaration

I hereby declare that I am the sole author of this thesis. This is a true copy of the thesis, including any required final revisions, as accepted by my examiners.

I understand that my thesis may be made electronically available to the public.

Abstract

Measuring the magnetic moment of a single spin remains an experimental challenge. Measuring such a moment at timescales relevant to relaxation in many small spin systems, even more so. However, such a measurement would permit detailed studies of the physics of these system and could probe new avenues of technology, such as real time use of single molecule magnets for quantum information processing. This thesis presents work towards realizing fast measurements of magnetic moments on the order of a single electron spin. This will be achieved by using a suspended carbon nanotube (CNT) resonator and a CNT-magnet coupling realized through nanoscale ferromagnets.

Fabricating high quality CNT resonators for this application requires combining high quality, high throughput nanofabrication with carefully adapted growth of CNTs. The first part of this thesis describes fabrication steps developed to create full wafer arrays of CNT devices consisting of predefined contacts and fine local gates that will provide the fine magnetic structure that will allow strong CNT-magnet coupling. The growth of CNTs over these contacts is iterated to achieve long defect-free CNTs suspended over the trench between contacts. Low temperature measurements of one such device allow identification of potential fabrication improvements.

The second section of this thesis describes simulations of the proposed sensing technique. Euler-Bernoulli beam models of the CNT allow extraction of resonant frequencies as a function of device parameters, and in particular allow us to identify the impact of a single Bohr magneton magnetic moment reversal. By mapping this frequency shift as a function of the device design and operating conditions we identify favourable device designs and optimal operating conditions to obtain maximum sensitivity. By comparing the achievable frequency shifts with intrinsic resonator noise, we calculate the fundamental signal to noise ratios of this sensing technique. By also considering transient response decay we extract optimal measurement bandwidths. These calculations reveal that magnetic switching on the order of a single Bohr magneton can be observed on timescales as short as 10 μs with this technique.

Acknowledgements

I would first like to thank my supervisor, Jonathan Baugh, for his invaluable guidance throughout this reasearch project. I must also thank Shirley Tang and Rob Hill for their guidance as part of my advisory committee. Additionally, I thank Hartwig Peemoeller for being a part of my thesis defense committee.

Next, I would like to thank the other CSG group members who have helped me along the way. Greg for answering my many questions and for performing metal deposition and etching of my devices. Sean, Chris, and Kaveh for the many helpful discussions and assistance with lab equipment and cryostat operation. Mustafa for your help getting my fabrication experience off the ground, and Grant for expanding our lab software.

I would also like to thank the Tang Lab members, particularly Andrew for the countless hours spent with me running CVD and helping me diagnose the many hurdles in getting my growths working. Mike, Tyler and Shirley were also always willing to help me with Raman and general growth diagnosis.

The devices presented in this thesis would not be possible without the QNCFab and its great staff. Thank you Nathan, Brian, Rod, and Vito, for keeping the QNCFab facility running smoothly and ever growing, and for providing invaluable advice for my fabrication process.

I would also like to thank Om and Ying for training me in the power of AFM and letting me in at all hours to measure another device.

This work was made possible by the support of NSERC, the Waterloo Institute for Nanotechnology, and by the generous funding of the lab equipment by NSERC, the Ontario Ministry for Research and Innovation and the Canadian Foundation for Innovation.

A special thank you to my friends and family, especially my parents for always supporting me and allowing me get to this point.

And a final thank you to Kirstin, for all that you do. You make it all possible.

Table of Contents

List of Tables

List of Figures

Chapter 1

Introduction

Understanding the physical behaviour of systems at the nanoscale is of great importance for gaining a fundamental understanding of nanoscale physics and applying these systems towards technological applications. Nanoscale phenomena are becoming increasingly relevant to current electronics research, and as we look to new avenues of technology such as quantum information processing, we seek to harness the quantum mechanical nature of these systems to realize new capabilities. Towards these applications, significant interest has been expressed in harnessing the magnetic degrees of freedom of nanoscale systems, such as the spin states of single molecule magnets [1]. Such nanomagnetic systems would have applications ranging from classical memory to quantum information processing.

One of the major challenges in determining the behaviour of nanomagnetic quantum systems comes from the inability to observe at the level of a single quanta. Advances in detectors such as quantum point contacts for charge sensing [2], and single photon detectors in optics[3], have enabled great expansion in the understanding and application of quantum behaviour in those fields. Magnetic sensing however, has thus far been primarily limited to ensemble measurements. There have been a few demonstrations of measurements at single Bohr magneton levels [4, 5, 6], however these each face unique limitations and are usually long time-averaged measurements that do not permit single shot state observation.

The earliest demonstration of single Bohr magneton magnetic moment sensitivity was achieved by magnetic resonance force microscopy (MRFM) [4]. In this technique, a small ferromagnetic tip on a cantilever oscillates in close proximity to the magnetic object of interest. The magnetic moment will be cyclically flipped, in phase with the resonator mo-

tion, through adiabatic rapid passage. The phase-locked magnetic oscillation will shift the resonant frequency of the cantilever via the force between the magnet and the ferromagnetic tip. Under the right conditions this technique can measure single electron spins, with magnetic moments of $m = \mu_B$. While the sensing ability of this technique has been well demonstrated, the need to drive resonance of the sample of interest and average over long measurement times (eg, 13 hours per data point in reference [4]) mean that this technique cannot be applied to real time sensing.

More recently developed techniques have been able to measure magnetic moments of a few Bohr magnetons without driving resonance in those spins [5, 6]. In the first experiment, a nanoscale superconducting quantum interference device (nanoSQUID) was assembled on the apex of a pulled quartz tip, resulting in an effective diameter as small as 46 nm. The small SQUID size allows it to measure magnetic flux generated by a single spin within ~ 10 nm of the nanoSQUID, with sensitivity down to $0.38\mu_B \mathrm{Hz}^{-1/2}$. However, the nanoSQUID sensitivity still requires ~ 1 second measurement averaging in the ideal case, and the allowable operating magnetic field is limited to $B \sim 1$ T. The second experiment (reference [6]) makes use of a carbon nanotube (CNT) resonator and torque exerted on anisotropic nanomagnets. This experiment is discussed further in section 4.1, however it can be noted here that the measurement uses non-linear resonance, thus limiting the measurement bandwidth, and requires anisotropic nanomagnets that can be aligned perpendicular to the applied fields, properties that many systems of interest will not exhibit.

The desired realization of fast readout of nanomagnet transitions will require a significant boost in sensitivity over previously demonstrated techniques. Towards this goal, we take a cue from other instances of large sensitivity improvements in mass [7, 8, 9, 10], and force [11] sensing, as well as the CNT-torque technique above [6], and explore the CNT resonator as a potential sensor for nanomagnets. The extremely small size of CNTs, combined with their unique mechanical and electrical properties make them a very powerful tool for high sensitivity measurements.

This thesis is organized as follows. Chapter 2 explains some of the relevant properties, behaviour, and operation of CNT resonators. Chapter 3 discusses nanofabrication techniques used to create suspended CNT devices, and presents measurements and analysis of fabricated devices to guide future fabrication. Chapter 4 explains the proposed nanomagnetic sensing technique and presents numerical simulations to quantify and optimize design and operation of these devices.

Chapter 2

Suspended Carbon Nanotubes

Nanoelectromechanical systems (NEMS) are devices combining mechanical and electrical behaviour at the nanoscale. Within the field of NEMS, single-wall carbon nanotube resonators present a particularly intriguing technology. Due to their extremely low mass and high Young's modulus, carbon nanotube NEMS have been able to achieve multiple orders of magnitude increases in sensitivities over similar NEMS in various sensing applications as mentioned in the previous section.

In applying the CNT resonator towards magnetic moment sensing, we will use a magnetic-moment dependent force to shift the resonant frequency of the CNT nanomechanical oscillations. This shift in resonant frequency will be observed as a change in the CNT conductance, due to the electromechanical coupling of suspended CNTs. This section describes the relevant behaviour of the CNT resonator, including electronic transport, mechanical properties of the resonator, common CNT resonator readout techniques, and how the noise of the CNT mechanical system will impact measurement limits.

2.1 CNT Electrical Transport

CNTs have unique transport properties, owing to both their 1D nature and the unique electronic band structure inherited from graphene. This section discussed the basics of CNT electrical transport and how it will play a role in our devices.

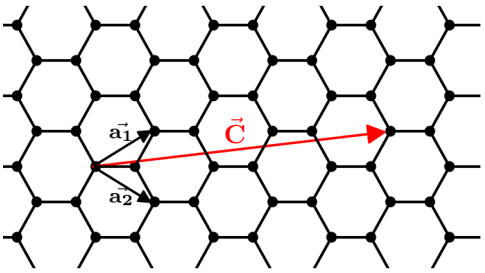

Figure 2.1: The direct lattice of graphene, including the primitive unit vector $\vec{a}_1$ and $\vec{a}_2$, and the chiral vector $\vec{C}$ that is used to define CNTs. In this figure $\vec{C} = 3\vec{a}_1 + 2\vec{a}_2 = (3, 2)$

2.1.1 Band structure of CNTs

Structurally, the CNT can be thought of as rolled sheet of graphene. Figure 2.1 shows graphene lattice with unit vectors, $\vec{a}_1$ and $\vec{a}_2$, and the chiral vector $\vec{C}$ that will define the CNT. The chiral vector represents the circumference of the CNT, such that the end points of $\vec{C}$ are the same point of the CNT. The chiral vector is specified by the integer multiples for each unit vector that make up $\vec{C}$

$$\vec{C} = n\vec{a}_1 + m\vec{a}_2 \equiv (n, m) \tag{2.1}$$

The CNT are categorized by their chiral vector. When $n = m$, the CNTs are armchair nanotubes, while $m = 0$ gives zigzag nanotubes. Both armchair and zigzag nanotubes are achiral, while any other (n, m) CNT is chiral.

The rolled graphene concept can also be used to estimate the band structure of CNTs, using the zone folding approximation [12]. Figure 2.2a shows the energy dispersion of the conduction band in graphene. The points K, K' are the points of the Dirac cones, at which the valence and conduction bands meet and a linear dispersion leads to massless carriers in graphene. The continuum of k_x and k_y values in graphene are a consequence of the near-infinite lateral dimensions of graphene. When the graphene is rolled up into a finite cylinder, periodic boundary conditions are imposed along the circumferential direction of the CNT. As a result, the circumferential wave vector component, $k_\perp$ will take discrete values, while the component along the CNT axis, $k_{||}$ will remain continuous.

The energy bands of the CNT correspond to the traces of these discrete $k_\perp$ values in

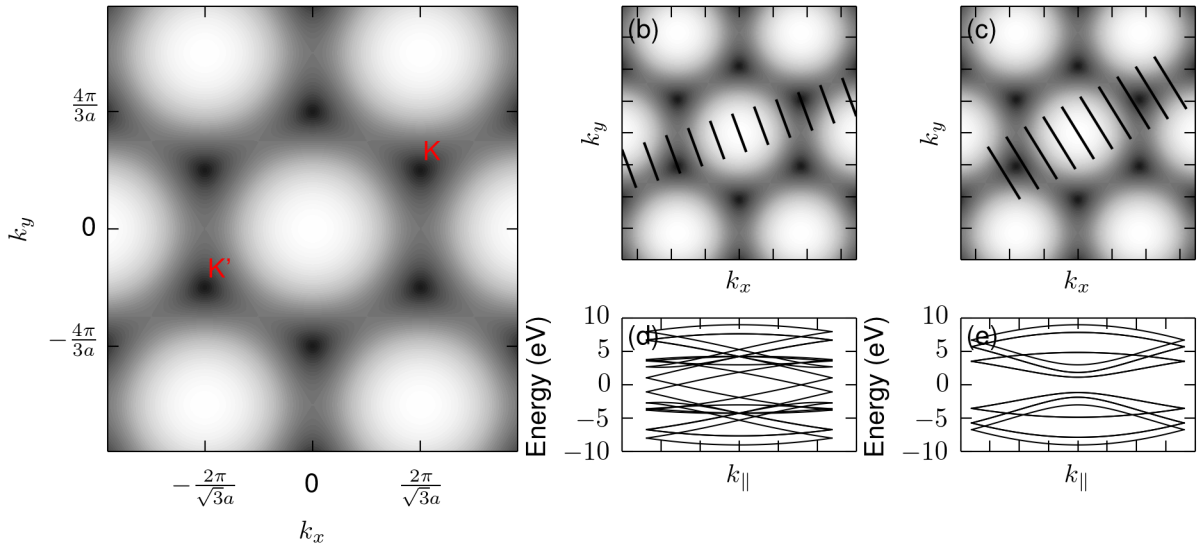

Figure 2.2: **a)** The energy dispersion of the conduction band of graphene, with darker regions being lower energy. The allowed $\vec{k}$ of the first Brillouin zone for a **(b)** (4,1) and **(c)** (5,0) CNT, displayed on the graphene conduction band dispersion. The subband energies of these CNTs are shown in **(d)** and **(e)**, respectively.

the graphene energy dispersion. The electrical properties of the CNT will depend on how these cuts align with the graphene dispersion. Figure 2.2b shows the case when $(n-m)$ is an integer multiple of 3, which results in some $k_\perp$ aligning with the Dirac points. In this case the conduction and valence bands of the CNT touch, as shown in figure 2.2d, and unlike graphene there is a finite density of states at this point, resulting in a metallic CNT. Figure 2.2c shows the case in which $(n-m)$ is not a multiple of 3, which results in no $k_\perp$ crossing through the dirac points. This leads to bandgap opening, as shown in figure 2.2e, and the CNT behaves as a semiconductor with an approximate bandgap of $E_g \approx 0.9\text{eV}/d$, where d is the nanotube diameter in nm.

The exact band structure of the CNT will differ slightly from the zone-folding approximation, primarily due to curvature effects of the CNT causing C-C bond elongation and mixing between π and σ orbitals of the carbon atoms. The main effect of this mixing at the low energies of interest to us, is an opening of a small bandgap in all metallic CNTs except for armchair nanotubes. The non-armchair metallic CNTs are labeled "quasi-metallic", or small-bandgap. The curvature induced bandgap is approximately 37 $\text{meV}/d^2[\text{nm}] \cdot \cos 3\theta$,

where θ is the angle between $\vec{C}$ and $\vec{a_1}$ [13, 14]. There can be additional bandgap opening in these small-bandgap CNTs due to strain that will further increase this bandgap by ~ 50 meV [14, 15].

The small bandgap CNTs are especially interesting for low temperature experiments, as the low effective carrier mass ($m^* \sim 0.014 m_e$ for 100meV bandgap CNT) leads to large level spacing and allows quantum dots to be formed in ~ 1 μm CNTs [14]. This, as well as high gate-ability and higher conductance at low temperatures, will make the small-bandgap CNTs the preferred type for our devices. Due to the probabilistic nature of the CVD growth process used to fabricate the CNT devices, a nearly even distribution of chiralities is created, and we expect $\approx 1/3$ of the CNTs to be small-bandgap.

2.1.2 CNT-Metal Contacts

CNT-metal contacts are known to form Schottky barriers in the majority of cases. The exact mechanism of the Schottky barrier formation is still debated [16]. One possible explanation, that agrees well with observations, is described here to illustrate the role of contact metal selection and treatment in CNT devices.

In normal metal-semiconductor interfaces, metal-induced gap states (MIGS) are created at the metal-semiconductor interface. There is a charge transfer with these states that leads to a dipole across the interface, and this dipole modifies the electrical potential, and thus the Schottky barrier, of the interface. This effect is known as Fermi level pinning, and as a result the Schottky barrier of metal-semiconductor interfaces is largely independent of the metal work function, in contrast to what is naively expected from the Schottky-Mott rule, in which the electron Schottky barrier is

$$\Phi_B^{(n)} = \Phi_{metal} - \xi_{sc} \tag{2.2}$$

where Φ_{metal} is the metal work function and ξ_{sc} is the electron affinity of the semiconductor.

In metal-CNT interfaces, Fermi pinning is much weaker or absent [17]. In side-contacted CNTs as we will use, this can be attributed to the extremely small dimension of the CNT wall. The depletion region which transfers charge to the metal-CNT interface is very small in the CNT, and thus only partial band realignment occurs. The partial realignment means that the actual Schottky barrier will be somewhere between the midgap value ($\Phi_B = E_g/2$) and the Schottky-Mott value of equation (2.2). One of the results of this behaviour is

that the contact properties for CNT-metal contacts depends strongly on the metal work function. High work function metals such as Pd have been experimentally shown to achieve Ohmic p-type contacts [18], while lower work functions metals such as Sc and Y have obtained Ohmic n-type contacts [19]. The Schottky barrier can also be effected by exposure of the device to air [20], hydrogen [18], or other conditions that either shift the metal work function or dope the CNT. Finally, the level of band realignment, and thus the size of the Schottky barrier, is dependent on the CNT diameter. For example, CNTs with diameter below 1.4nm are not expected to form ohmic contacts with Pd, while those of higher diameter can [21, 22].

Additionally, there is often an extra tunneling barrier in series with the Schottky barrier. This additional barrier is a result of an imperfect CNT-metal interface [20], possibly as a result of oxidization or poor wetting of the CNT by the metal [23]. Platinum has a higher work function than palladium, but makes more resistive contacts with similar fabrication [18] due to poor CNT wetting [24].

2.1.3 Low temperature transport

At cryogenic temperatures, single electron transport and quantum confinement can become relevant to CNT transport. The Schottky and additional tunneling barriers of a Pt-contacted CNT will provide electron confinement that can lead to Coulomb blockade within the CNT channel. The low effective mass of electrons in the CNT can lead to quantum dot formation in micron long CNTs, as mentioned in section 2.1.1.

A quantum dot is comprised of an island connected to a source and drain electrode through tunnel barriers, with the tunneling condition requiring that the contact resistance satisfies $R_c \gg h/e^2$ [25]. The potential of the island is tuned by a separate gate electrode that is capacitively coupled to it. Due to the discrete nature of the electron charge, the island charging energy is incremented by $U_C = e^2/C$, where e is the electron charge and $C = C_s + C_g + C_d$ is the total capacitance of the island-system. When $U_C \ll k_B T$, the discrete charging energy spectrum leads to Coulomb blockade. Figure 2.3a and 2.3b shows two distinct states of the quantum dot for small bias, V_{sd}. In 2.3a, the states below the chemical potentials of the source and drain are filled while every unfilled state is above the source/drain chemical potentials. In this case there are no available states for electrons to tunnel into, and thus no current will flow through the island. In figure 2.3b, one of the

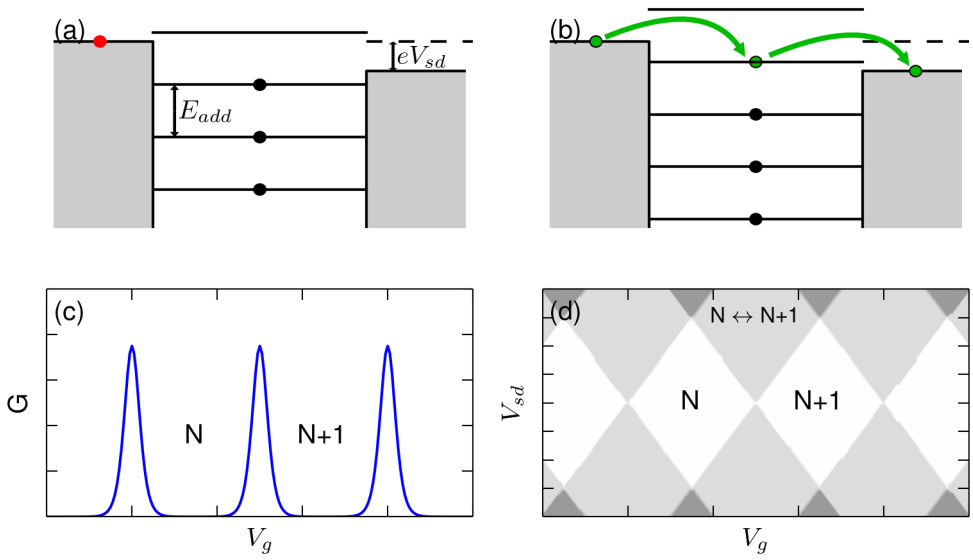

Figure 2.3: **a)** A quantum dot, in which the filled states of the leads (grey regions) are tunnel coupled to the discrete energy states of the dot. This dot is in the Coulomb blockade regime, in which no energy level (separated by E_{add}) is available in the bias window, eV_{sd}. **b)** Conduction through the quantum dot occurs when one of the energy levels is within the bias window. **c)** At low bias voltages a quantum dot exhibits Coulomb peaks in conduction. In between these peaks the electron number on the island is fixed, denoted by the electron occupation numbers, N and $N+1$. **d)** The conduction of a quantum dot as a function of V_{sd} and V_g shows Coulomb diamonds, regions of zero conductance.

discrete charging states is in the bias window. In this case, an electron in that state will tunnel out to the drain, and electrons in the source can tunnel into the dot. This leads to a finite current that will depend on the tunneling rates through the barriers, and the characteristic peak in low bias conductance, shown in figure 2.3c, is called a Coulomb peak.

At higher bias, the window between contact potentials opens, and eventually will reach a point where there will always be at least one allowed energy level, and thus current, for any gate voltage. This dependence on bias and gate voltage lead to the Coulomb diamond pattern shown in figure 2.3d. The Coulomb diamond size and edge slopes can be used to determine the capacitances (C_s,C_d,C_g) and charging energy scales of the island [26].

When the quantum dot is small enough, quantum confinement can cause discrete elec-

tron energy levels. When these energy levels become comparable to the thermal energy, $\Delta E \gtrsim k_B T$, the energy required to add an electron to the dot, E_{add}, will be a combination of the charging and electron energy, $E_{add} = U_C + \Delta E$, where $\Delta E = E_{n+1} - E_n$ is the electron energy level spacing for the next electron. When there are degeneracies in the electron energy levels, such as a spin degeneracy, the Coulomb peaks can be unevenly spaced as ΔE changes from 0 between degenerate states to a finite value once an energy level is filled. In CNTs, there is both a spin and valley degeneracy, and thus a four-peak pattern is expected for ideal CNT quantum dots. The four peak Coulomb diamond pattern has been observed experimentally for clean individual CNTs[27].

2.2 Mechanical properties of suspended CNTs

One of the defining characteristics of the CNT NEMS is its extremely low mass. The linear mass density of a 1 nm diameter CNT is $\rho A = \rho_G \pi d = 2.4 \cdot 10^{-15}$ kg/m, where $\rho_G = 7.7 \cdot 10^{-7}$ kg/m^2 is the area density of graphene. Then, a 1 μm long CNT with a 1 nm diameter will have a mass of $2.4 \cdot 10^{-21}$ kg, several orders of magnitude smaller than the mass of other typical NEMS devices ($m \gtrsim 10^{-17}$ [28]). Critically for our applications, the small mass means that a relatively soft spring constant device can still have a high resonance frequency, approximating this relation by the simple harmonic oscillator relation $\omega_0 = \sqrt{\frac{k}{m}}$. This allows a high resonance frequency and a large response to applied forces.

The other commonly cited advantage of the CNT NEMS is its high Young's modulus, $E \approx 1 - 1.3$ TPa [29, 30]. The high Young's modulus allows the CNT to act as a beam resonator despite its small diameter, as the bending rigidity $D = EI$ remains high despite the small area moment of inertia $I = \pi r^4/4$. The combined high Young's modulus and small mass have allowed fabricated CNT devices to achieve fundamental resonance frequencies as high as 280 GHz [31]. Furthermore, the high strength of the CNT allows a large tuning of resonance frequencies by applying static forces to the CNT. In particular, the CNT can be switched from beam-like bending in which intrinsic properties dominate the resonance frequency, to string-like bending in which the applied tension dominates [32].

As a final note on the mechanical behaviour of the CNT resonator, it is typically a very high aspect ratio device, with $L : d \sim 1000 : 1$. One result of this is that it is often possible to drive CNT resonance of a greater amplitude than the CNT diameter. At this

oscillation amplitude non-linear effects become important and the CNT can be treated as a Duffing oscillator with bistable resonances [32]. The non-linear oscillator behaviour can be used to facilitate sensitive readout by tuning to a bistable point and looking for transitions between the two stable oscillation amplitudes [6].

2.3 Mechanical-Electrical Coupling

The mechanical-electrical coupling to the bending mode of a CNT resonator is due to the mechanical modulation of the gate capacitance causing changes of the induced charge on the CNT [33]. The capacitance between the CNT and an adjacent gate is modelled as a wire parallel to a plate

$$C_g(x) = \frac{2\pi\epsilon_0 L}{\operatorname{arccosh}((h+x)/r)} \tag{2.3}$$

where L is the CNT length, h is the equilibrium CNT-gate separation, x is the CNT displacement from equilibium, and r is the CNT radius. The gate induced charge on the CNT is $q = C_g V_g$. The electrostatic attraction between this induced charge and the gate gives the electrostatic force on the CNT [34]

$$F_{elec} = \frac{1}{2} C_g' V_g^2 \tag{2.4}$$

where $C_g' = \frac{\partial C_g}{\partial x} \approx -\frac{2\pi\epsilon_0 L}{(h+x)\ln^2(2(h+x)/r)}$, with the approximation using $(h+x)/r \gg 1$.

The electrostatic attraction is used to tune the mechanical resonance and simultaneously drive it. Applying a DC gate voltage will pull the CNT towards the gate, increasing tension and thus resonant frequency (for further details see Chapter 4). In combination with the DC voltage, a small AC component is applied to the gate so that the total gate voltage is $V_g = V_g^{dc} + V_g^{ac}(t)$, with the condition that $\left|V_g^{ac}\right| \ll V_g^{dc}$. To first order, this creates an AC force on the CNT, $F^{ac}(t) \approx \frac{1}{2} C_g' V_g^{dc} V_g^{ac}(t)$. The AC signal can be used to drive mechanical resonance.

2.4 Readout of mechanical motion

The mechanical motion of a suspended resonator is measured by observing the electrical conduction through the CNT in some manner, using the coupling described in the previous

section. The conductance of the CNT will be proportional to the induced charge $q = C_g V_g$, allowing mechanical modulation of C_g to be measured as conductance modulation.

Directly measuring the conductance oscillations in the CNT is challenging, as the high resistance of the CNT channel, combined with realistic capacitances in the measurement system will cause high-frequency signals to be too weak to measure. In particular, the cut-off frequency of the system is given by [32]

$$\omega_c = \frac{1}{R_{\|} C_{readout}} \tag{2.5}$$

where $R_{\|} = 1/(1/R_{CNT} + 1/R_{readout})$ is the resistance of the CNT-readout system, with $R_{readout}$ the readout circuit impedance, and $C_{readout}$ the effective readout capacitance. Typical estimates of these values at room temperature are $R \approx 50$ kΩ and $C_{readout} \sim 10pF$, resulting in $\omega_c \sim 2$ MHz, which is lower than the expected resonance frequencies of micron long CNT resonators ($\omega_0 \sim 10 - 100$ MHz). Thus, readout of the CNT motion will require some form of down-mixing or current rectification to be used.

The main readout techniques used for CNT resonators are presented below. First we discuss common room-temperature techniques using various mixing methods, then we discuss low temperature measurements that primarily rely on DC rectification. Finally we discuss recent demonstration of room temperature readout with optimized cutoff frequencies, ω_c, that greatly improves the available measurement bandwidth, which will be important for our desired magnetic moment sensing.

2.4.1 Two Source Mixing

The original method of sensing CNT mechanical motion [35] makes use of the CNT resonator as a two-source mixer. In the two-source mixing technique, the gate voltage has an AC component that oscillates at frequency ω, and the bias voltage is an AC voltage oscillating at offset frequency $\omega + \delta\omega$.

Writing $V_g = V_g^{dc} + V_g^{ac}(t)$ and $C_g = C_g^{dc} + C_g^{ac}(t)$, where $C_g^{ac}(t)$ is a result of the mechanical motion of the CNT.

$$C_g^{ac}(t) \approx \left.\frac{\partial C_g}{\partial x}\right|_{x=0} x(t) \tag{2.6}$$

where $x(t)$ is the displacement of the CNT from equilibrium averaged along the CNT axis.

The conductance of the CNT can be written

$$G = \frac{\partial G}{\partial q} q = \frac{\partial G}{\partial q} C_g V_g \approx \frac{\partial G}{\partial q} \left(C_g^{dc} V_g^{dc} + C_g^{ac} V_g^{dc} + C_g^{dc} V_g^{ac} \right) \tag{2.7}$$

$$\approx \frac{\partial G}{\partial q} \left(C_g^{dc} V_g^{dc} + \left. \frac{\partial C_g}{\partial x} \right|_{x=0} x(t) V_g^{dc} + C_g^{dc} V_g^{ac} \right) \tag{2.8}$$

where the first approximation is to first order in the small terms V_g^{ac} and C_g^{ac}. Note that the conductance modulation can be calculated from experimentally accessible values as $\frac{\partial G}{\partial q} = \frac{\partial G}{\partial V_g} \frac{1}{C_g}$.

Writing $V_g^{ac}(t) = V_g^{ac} \cos(\omega t)$ and setting the source-drain voltage to be $V_{sd} = V_{sd}^{ac} \cos((\omega + \delta\omega)t + \phi_{sd})$, gives a current through the CNT of

$$I = G V_{sd} = \frac{\partial G}{\partial q} \left(C_g^{dc} V_g^{dc} + \left. \frac{\partial C_g}{\partial x} \right|_{x=0} x(t) V_g^{dc} + C_g^{dc} V_g^{ac} \cos(\omega t) \right) V_{sd}^{ac} \cos((\omega + \delta\omega)t + \phi_{sd}) \tag{2.9}$$

For small amplitude oscillations, the CNT response can be approximated as a simple harmonic oscillator response

$$x(t) = \frac{F_d/m}{\sqrt{\left(\omega_0^2 - \omega^2\right)^2 + \omega^2 \omega_0^2 / Q^2}} \cos(\omega t + \phi) \tag{2.10}$$

where $F_d \approx C_g' V_g^{dc} V_g^{ac}$ is the AC driving force from the gate modulation, ω_0 is the resonant frequency, Q is the quality factor, and ϕ is a phase resulting from regular simple harmonic oscillator phase response and the details of tunneling and charging of the CNT [36].

The current at the mixing frequency $\delta\omega$ will then be

$$I_{\delta\omega} = \frac{\partial G}{\partial q} V_{sd}^{ac} \left(\frac{(V_g^{dc} C_g')^2 V_g^{ac}}{2m\sqrt{\left(\omega_0^2 - \omega^2\right)^2 + \omega^2 \omega_0^2 / Q^2}} \left(\cos(\delta\omega t + \phi_{sd}) \cos(\phi) + \sin(\delta\omega t + \phi_{sd}) \sin(\phi) \right) + \frac{1}{2} C_g^{dc} V_g^{ac} cos(\delta\omega t + \phi_{sd}) \right) \tag{2.11}$$

The first term in equation (2.11) is the result of mechanical motion of the CNT, while the second term is a purely electrical term that is present in the absence of CNT motion.

Mechanical motion of the CNT is measured by distinguishing the sharp peak in I vs. ω associated with the first term, which has a full-width half-maximum of ω_0/Q.

Modified mixing techniques

There are a number of techniques similar to the two-source mixing, that make use of modifications of the driving signal to obtain a simpler experimental setup or higher signal to noise. For example, the amplitude modulation technique uses an amplitude modulated signal at the source contact to obtain the same effect as equation (2.11) at the amplitude modulation frequency, allowing only one high frequency signal to be required [36]. For a full description and comparison of these techniques see reference [32].

2.4.2 Frequency Modulation

One important modification of the mixing technique that we will explicitly discuss is the use of a frequency modulated driving signal. As mentioned above, the mixing technique has a purely electrical component at the measurement frequency. This can make readout more challenging, as it introduces an additional signal that doesn't carry desired information, and additional noise. Frequency modulation mixing eliminates this component, allowing for a purely mechanical signal [37, 38].

In this technique, a frequency modulated source-drain voltage is given as

$$V_{sd}^{fm} = V_{sd}^{ac} \cos\left(\omega t + \frac{\Delta\omega}{\Omega}\sin(\Omega t)\right) \tag{2.12}$$

where $\Delta\omega$ is the modulation strength and Ω is the modulation frequency. The FM signal can be decomposed in the Jacobi-Anger expansion, as an infinite sum of oscillations at frequencies $\omega \pm n\Omega$. The mixing current at Ω can then be calculated as[37]

$$I_\Omega = \frac{1}{2}\frac{\partial G}{\partial V_g} V_g^{dc} \frac{C_g'}{C_g} V_{sd}^{ac} \Omega \frac{\partial x}{\partial \omega} \tag{2.13}$$

which is only present when there is a mechanical response of the resonator. It should be noticed that the FM modulation couples the current to $\frac{\partial x}{\partial \omega}$, rather than directly to x, so that $|I_\Omega|$ is maximum on the edges of the resonant peak, $\omega = \omega_0 \pm \omega_0/Q$.

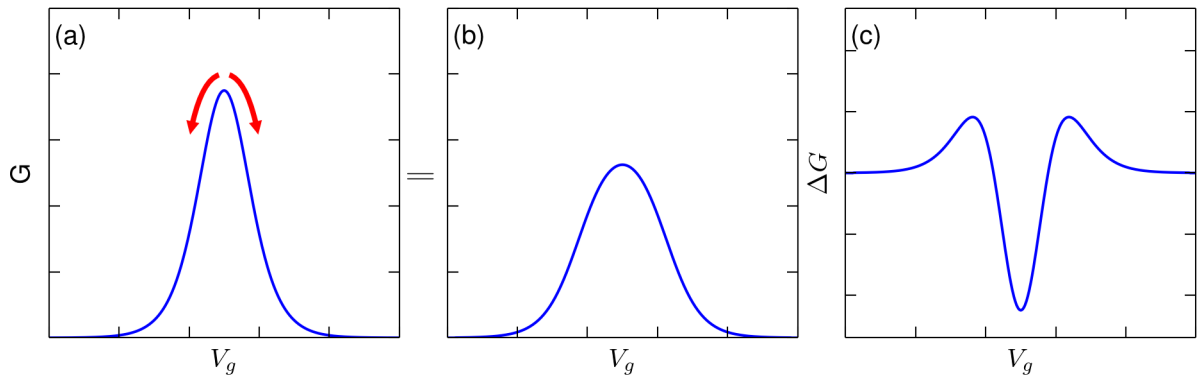

Figure 2.4: **a)** A Coulomb peak of a stationary CNT. The oscillation of the CNT will broaden the peak via averaging with respect to V_g. **b)** The broadened Coulomb peak due to CNT motion. **c)** The change in DC conductance that occurs as a result of CNT motion.

2.4.3 Coulomb blockade enabled DC readout

Low temperature measurements of the CNTs can take advantage of Coulomb blockade in the CNT to observe the mechanical CNT oscillations in a DC current measurement, as originally proposed in Reference [39]. As described in section 2.1.3, at low temperature a series of sharp Coulomb peaks will form in the CNT conductance, G, as a function of V_g. The mechanical motion of the CNT will cause oscillations in the effective V_g. These oscillations act to broaden the Coulomb peaks, as shown in figure 2.4a and 2.4b. By observing the conductance at a fixed point on the Coulomb peak, the mechanical oscillations can thus be seen as a change in the conductance, resulting from the peak broadening, shown in figure 2.4c. The current through the CNT will be given by

$$I_{motion} = I_{stationary} + \left(\frac{x_{max}}{2}\frac{C_g'}{C_g}V_g\right)^2 \frac{\partial^2 I}{\partial V_g^2} + O(x_{max}^4) \tag{2.14}$$

where $I_{stationary}$ is the current in the absence of CNT motion, and x_{max} is the maximum amplitude of the CNT motion.

2.4.4 Ultrasensitive correlation measurements

While basic DC rectification Coulomb blockade measurements can provide simple resonator measurements at low temperatures, the noise caused by the required amplifiers does not

allow maximum sensitivity of CNT resonator measurement. An ideal measurement scheme for resonators would be limited only by the noise of the resonator itself. That is, the measurement of the CNT resonator frequency or amplitude would be able to observe the thermomechanical noise of the mechanical resonator (See section 2.5). A measurement at the thermomechanical limit of a CNT resonator was recently demonstrated at 1.2 K [11], and is described here.

This measurement scheme makes use of the same C_g modulation as the DC rectification scheme, but uses cross-correlated electrical measurements to reduce electrical noise. The electrical measurement scheme was originally presented in [40]. It uses two independent low noise, high-impedance voltage amplifiers to measure the current through the CNT, which is converted to voltage via resistor. The outputs of the independent amplifiers are then input into a fast Fourier transform signal analyser to measure the cross-correlation of the amplifier signals. This technique removes the voltage noise introduced by the amplifiers, allowing much better signal to noise ratios. However, this measures the cross correlation of the current signal, so it is used to extract the power spectral density of the current, $S_I = \langle \delta I \rangle / W$, where W is the measurement bandwidth and $\langle \delta I \rangle$ is the mean square measured Fourier component at frequency $\sim |\omega_{sd} - \omega|$ [11]. As shown in reference [11], this can be used to measure the motion of the CNT at its thermomechanical limit. Additionally, the extracted power spectrum can be analyzed to determine the separate broadening mechanisms, and in particular the behaviour of resonant frequency fluctuations can be extracted even in the presence of dominant thermomechanical noise [41].

2.4.5 High frequency two source mixing

As mentioned in the introduction of section 2.4, the CNT circuit acts as a low-pass filter that does not permit current measurement at the CNT resonant frequency. One theoretically simple but practically challenging method to overcome this is to increase the cut-off frequency by decreasing $R_{\|}$ or $C_{readout}$. To permit measurable electrical signals, $R_{readout}$ should be similar to R_{CNT}, and thus $R_{\|}$ is essentially fixed by the CNT itself. Thus, the parameter of interest for optimizing ω_c is the readout capacitance of the measurement circuit. This optimization has been employed in one case to measure the resonant motion response of a suspended CNT at sub-microsecond time scales at room temperature [42].

The measurement method is very similar to regular two-source mixing measurements,

however the drain of the carbon nanotube is now converted to a voltage via a nearby resistor and this voltage is applied to the gate of a nearby high electron mobility transistor (HEMT) amplifier. The HEMT amplifier is located as close as possible to the CNT to minimize the capacitance of the readout circuitry, thus permitting high frequency signals to be transmitted to the HEMT gate. This allows the frequency offset of the two source method, $\Delta\omega$ to reach $\sim$ 10MHz, similar to the mechanical resonant frequency of the CNT. In reference [42], the HEMT signal was fed into a lock-in amplifier and integrated over timescale τ, with distinguishable measurements achieved for τ = 780ns. It should be noted that while this measurement was performed at room temperature, the technique is extendable to low temperature [42].

This fast readout could enable finer measurement of CNT noise processes, transient decay of CNT motion, and most importantly for the present work it could enable CNT resonators to be used to measure forces changing at submicrosecond timescales, thus permitting observations of the spin dynamics of nanomagnets.

2.5 CNT Resonator Noise

The ultimate limit on electromechanical measurements of CNT resonators will be determined by the intrinsic noise of the resonator, which is dominated by thermomechanical noise [43, 11]. As described above, the ultrasensitive measurement technique already allows measurement at this intrinsic noise floor at 1.2 K. It should be noted that single-electron tunnelling effects which often dominate low temperature CNT resonator damping [32] can be reduced with improved tunnel coupling, and in particular, can be eliminated by working in the hole transport regime of the CNT [44].

The thermomechanical noise in mechanical resonators is described by a stochastic force acting on the resonator that results in thermal equilibrium satisfying [45, 43]

$$\langle E_{kin} \rangle = \frac{1}{2} k_B T \tag{2.15}$$

$$\frac{1}{2} m' \omega_0^2 \langle x_{cm}^2 \rangle = \frac{1}{2} k_B T \tag{2.16}$$

where m' is the effective mass of the resonator, ω_0 is the resonant frequency of the fundamental mode, and $\langle x_{cm}^2 \rangle$ is the time average of the squared amplitude of the center of mass displacement.

This gives that the spectral density of the noise force is

$$S_F(\omega) = \frac{4k_B T m' \omega_0}{Q} \tag{2.17}$$

where T is the temperature at the resonator and Q is the resonator quality factor.

The noise force will cause a fluctuating amplitude response with spectral density

$$S_x(\omega) = \frac{4k_B T \omega_0}{m' Q\left((\omega^2 - \omega_0^2)^2 + \omega^2 \omega_0^2 / Q^2\right)} \tag{2.18}$$

The amplitude response can be approximately represented as a frequency fluctuation, with spectral power density [43]

$$S_\omega(\omega) \approx \left(\frac{\omega_0}{2Q}\right)^2 \frac{S_x(\omega)}{\langle v_{max}^2 \rangle} \tag{2.19}$$

$$= \frac{k_B T \omega_0^3}{m' Q \langle v_{max}^2 \rangle \left(Q^2(\omega^2 - \omega_0^2)^2 + \omega^2 \omega_0^2\right)} \tag{2.20}$$

where ω_0 is the resonant frequency, Q is the resonator quality factor, and $\langle v_{max}^2 \rangle$ is the mean square amplitude of the oscillatory motion of the driven resonator at its point of maximum displacement.

When using the CNT resonator as a magnetic force sensor, we will be interested in distinguishing small frequency shifts. The minimum detectable frequency shift that can be observed in the presence of the above frequency noise is given by [43]

$$\delta\omega_0 = \sqrt{\int_0^\infty S_\omega(\omega) H(\omega) d\omega} \tag{2.21}$$

where $H(\omega)$ is the transfer function of the measurement set-up. For simplicity we can approximate $H(\omega)$ as a square transfer function which is equal to one within $\omega_0 \pm \frac{1}{2\tau}$, and zero outside, where τ is the measurement averaging time. Then,

$$\delta\omega_0 = \sqrt{\int_{\omega_0 - 1/2\tau}^{\omega_0 + 1/2\tau} S_\omega(\omega) d\omega} \tag{2.22}$$

When the measurement averaging time satisfies $\tau \gg \frac{Q}{\omega_0}$, $S_\omega(\omega)$ is approximately equal to its maximum value over the full integral range and we can approximate

$$\delta\omega_0 = \sqrt{\frac{k_B T}{m' \left\langle v_{max}^2 \right\rangle \tau \omega_0 Q}} \tag{2.23}$$

where the effective resonator mass is calculated as $m' = m\left(\frac{1}{L}\int_0^L v^2 dz\right)/v_{max}^2$. In the limit that the measurement averaging time goes to zero, we can substitute $H(\omega) = 1$ into equation (2.21) and obtain

$$\delta\omega_0|_{\tau\approx 0} = \sqrt{\frac{\pi k_B T}{2m' \left\langle v_{max}^2 \right\rangle Q^2}} \tag{2.24}$$

For later convenience we can also re-express these values in terms of natural frequency. When $\tau \gg \frac{Q}{2\pi f_0}$

$$\delta f_0 = \frac{1}{2\pi}\sqrt{\frac{k_B T}{2\pi m' \left\langle v_{max}^2 \right\rangle \tau f_0 Q}} \tag{2.25}$$

and for $\tau \to 0$

$$\delta f_0|_{\tau\approx 0} = \frac{1}{2\pi}\sqrt{\frac{\pi k_B T}{2m' \left\langle v_{max}^2 \right\rangle Q^2}} \tag{2.26}$$

Chapter 3

Device Fabrication and Analysis

This chapter details cleanroom fabrication methods for realizing high quality suspended CNT devices, for the goal of magnetic force sensing experiments. To realize the maximum benefits of CNT NEMS, mechanical quality of the CNT devices is critical. To keep the CNT free of any contaminants or defects, and thus maximize the resonator quality, the CNTs must be grown as the last step in the fabrication process, removing any interaction with processing chemicals and treatments [39]. In this method of fabrication, the required gates, trenches, and contacts are defined, followed by patterning of the CNT catalyst, and finally chemical vapor deposition(CVD) growth of the CNT on top of these features.

Due to the probabilistic nature of the CNT growth, including both the CNT location and properties, the post-fabrication CVD technique does not in practice obtain high device yields. We estimate a best-case yield for small-bandgap suspended devices of $\sim 5\%$ on pre-patterned devices, for the device geometry that will be described below [46]. To overcome the low yield, a large number of pre-patterned devices are required. To allow fabrication of a large number of potential devices, full wafer processing is used when feasible.

This chapter describes the overall device process, then details the techniques used in fabrication. In particular, the CVD growth of CNTs is described and iterative improvement of device growth is presented. Finally, low temperature measurements of some finished devices are presented to obtain a preliminary indication of device quality.

3.1 CNT Device Process

The suspended CNT device fabrication process is described below. The techniques used in this fabrication will be discussed in 3.2 and 3.3. A fully detailed description of the nanofabrication process is given in appendix A.

1. Start with a 4" intrinsic silicon ($\rho > 5000\ \Omega$/cm) wafer with 300 nm of thermal SiO_2
2. Deposit 10 nm Ti/40 nm Pt source-drain contacts (Black pattern in figure 3.1a) using bilayer photolithography and E-beam evaporation
3. Etch the trench between the source-drain contacts (Green pattern in figure 3.1a) using monolayer photolithography and dry etching
4. Deposit 10 nm Ti/40 nm Pt gate pads (Red pattern in figure 3.1a) using bilayer photolithography and E-beam evaporation
5. Deposit 10 nm Ti/40 nm Pt fine gate patterns, or a ferromagnetic metal in the case of the actual device, using EBL (example device in figure 3.1c) and E-beam evaporation
6. Deposit catalyst islands (Blue pattern in figure 3.1a) using method described in section 3.3.2
7. Grow CNTs via chemical vapor deposition (see section 3.3)

A finished device is shown in figure 3.1c.

3.2 Nanofabrication techniques

The following nanofabrication tools are used to define the CNT devices.

Figure 3.1: **a)** The photomask patterns used for CNT device fabrication, where the scale bar is 10 μm. **b)** A device with source-drain contacts, trench etching, and gate pads, where the scale bar is 10 μm. **c)** A finished device, after CVD growth, showing the EBL-defined fine gate and photolithography-defined catalyst islands, where the scale bar is 5 μm.

3.2.1 Photolithography

Large ($> 2\mu$m) device features can be readily patterned via contact photolithography. In general photolithography, an ultraviolet(UV)-sensitive photoresist is deposited onto the sample, often via spinning to achieve uniform thickness, followed by a patterning step. The patterning step is done by placing a mask in contact with the sample, then exposing the assembly to high levels of UV light. The masks serves to protect some regions of resist from the UV light, thus forming a copy of the mask in the resist exposure levels. After the exposure step, the pattern is developed in specially tailored solvents, such that the exposed regions of resist are dissolved while the unexposed regions remain.

After the pattern is developed, the desired processing (eg, etching or metallization) can be completed over the full wafer. The exposed sample regions will be subjected to the processing, while the resist will protect the covered regions. After all processing is complete, the remaining photoresist is dissolved in a lift-off solvent, leaving behind the desired metal or etching patterns on the device substrate.

Bilayer Photolithography for Metallization

Standard single layer photolithography can have difficulties with lift-off processing. Figure 3.2a shows a cross section of a wafer after typical single layer resist development, highlighting that the positive photoresist walls usually have a slightly positive slope (85 ° to 89 °) [47]. Figure 3.2b shows the same cross section after metal is deposited. Even for

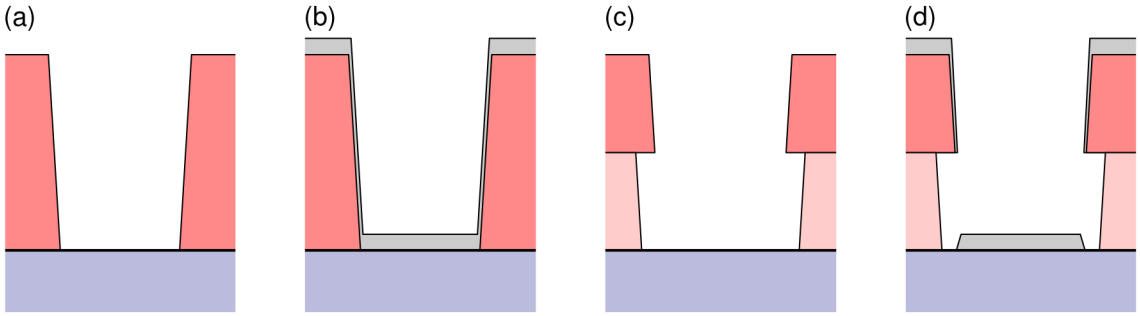

Figure 3.2: **a)** A cross section of single layer photoresist after development, and **b)** after metal deposition. **c)** A cross section of bilayer photoresist after development, and **d)** after metal deposition

metal layers much thinner than the resist, there is the potential for semi-continuous metal connections going up the sidewall of the pattern. This can result in the metal on the resist not being removed during liftoff as desired, often leaving metal deposited on the sample in undesired locations. Due to the fine photolithography resolution that will be used in the CNT device fabrication and the need for high yield, we want to avoid these potential lift-off difficulties.

To overcome this issue, a bilayer resist can be used, in which the underlying layer develops more quickly than the top layer. Figure 3.2c shows a cross section of such a bilayer after development. Figure 3.2d shows this cross section after metallization. The step in the resist now eliminates the possibility of metal connection up the side wall, thus allowing reliable liftoff.

3.2.2 Electron Beam Lithography

The resolution of photolithography is limited by Fresnel diffraction [47]. For the Suss-Microtec MA6 mask aligner and resists used in our device fabrication, this limits the spacing between adjacent patterns to approximately 1μm. The fine gates that will be required for our CNT devices are on the order of several hundred nanometers wide, thus electron beam lithography (EBL) is required. In EBL, the sample is first coated with an electron-sensitive resist, such as polymethyl methacrylate (PMMA). Then, a focused beam

of electrons is scanned over the sample in a desired pattern. The sample is then developed to dissolve the resist regions which were subject to a high electron beam dose. Further processing then follows as in photolithography. Bilayer processing is also available for EBL, analogous to photolithography.

3.2.3 Metal Deposition

The metal films used in our devices are deposited using an IntlVac Nanochrome II-UHV electron beam evaporation system. A crucible containing the metal to be deposited is placed at the bottom of the chamber and the sample is placed inverted at the top of the chamber. Then, under ultrahigh vacuum, an electron beam is focused on the metal in the crucible, evaporating it. The evaporated metal atoms flow to the substrate where they form a thin film. The typical depositions rates used in our devices are 3 Å/s for Ti and 1 Å/s for Pt, allowing for smooth thin films to be deposited to a desired thickness.

3.2.4 Dry Etching

For CNT resonator devices, we need to form a trench between the source and drain contacts. To keep the CNT resonator from collapsing onto the substrate, we require the substrate to be completely removed between the contacts. We also want to avoid removing the substrate from below the contacts which can cause extra resonant signals due to contact vibration. These requirements can be satisfied by using the source and drain contacts as a mask for an etch with no lateral effect, such as a reactive ion (dry) etch.

The dry etching of these devices is performed by an Oxford Instruments ICP380 plasma-based dry etching system. The etching is performed by exciting reactive gases with an RF-field in a vacuum chamber[47]. The excited gas molecules are highly reactive and, in the case of SiO_2 etching as we are doing, the reactive molecules have stronger bonding than the Si-O bonds, and are thus able to remove the oxide material. Additionally, the ionic species generated during the etching procedure are accelerated by the RF field, bombarding the surface at normal incidence and providing directional energy transfer, resulting in anisotropic etching, and thus nearly vertical sidewalls of the resulting etch.

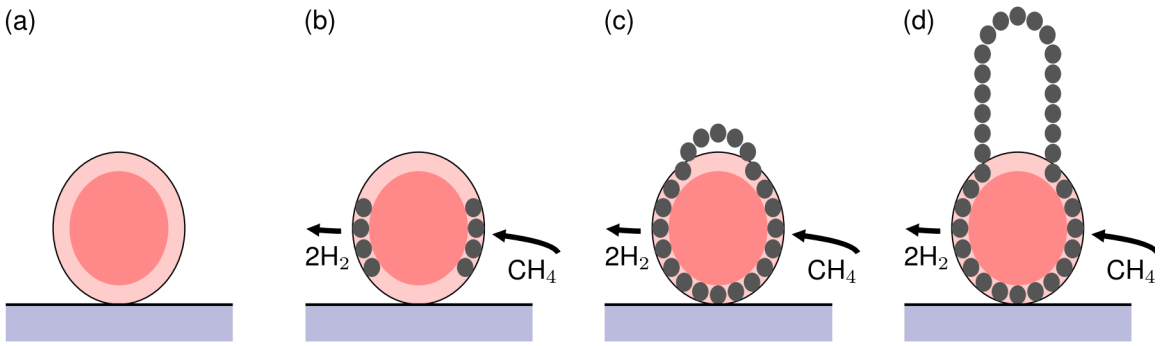

Figure 3.3: The growth mechanism of CNTs in CVD, as described in [48]. **a)** The catalyst nanopartical is shown on a supporting substrate. **b)** Catalytic decomposition and carbon absorption results in carbon atoms on the outer shell of the catalyst. **c)** Eventually the carbon over-saturates the particle and begins to grow off. **d)** The offshoot extends, forming a CNT.

3.3 CVD Growth of Suspended CNTs

Chemical vapor deposition (CVD) is used to grow the CNTs for these devices. CVD methods allow the CNTs to be grown in place, at intermediate temperatures (600 °C - 1000 °C). Growing the CNTs on the contacts, as enabled by CVD, allows very clean CNTs to realize high quality resonator and electrical behaviour.

3.3.1 CVD of CNTs

In the basic CNT CVD process, a hydrocarbon precursor such as CH_4 or C_2H_4 reacts with a transition metal catalyst to preferentially form CNTs [48]. The catalyst nanoparticles are deposited onto the sample to be grown. The sample is then placed in a CVD chamber and heated to 600 °C - 1000 °C. The precursor, along with other gases as needed for the particular process, are flowed into the chamber through mass flow controllers. The precursor is chemically decomposed by the catalyst, and the resulting carbon atoms are absorbed onto the nanoparticle. Eventually the nanoparticle surface saturates and additional carbon nucleates and grows the CNT, as depicted in figure 3.3.

A prime benefit of CVD is that thermal decomposition of the precursor is minimal, and decomposition occurs primarily at catalysts [48]. This allows for catalyst-free sites that are not active in the growth. This permits patterning of the CNT growth, to nominally allow CNTs only in select locations. In the devices discussed in this thesis, this is used to grow CNTs at the trench location while keeping the rest of the device free of both catalyst material and CNTs.

The mechanisms governing CNT CVD, particularly those which permit long and aligned (LA) CNT growth, are not universally agreed upon. Initial realizations of LA tubes used either raised catalyst terraces [49] or "fast heating" of the growth samples [50], leading to the hypothesis that local turbulence at the catalysts was required to grow long CNTs. Subsequent studies showed that neither of these methods are sufficient for obtaining LA tubes, and such CNTs can be achieved in regular CVD without terraces, provided the right catalyst pretreatment and process gas combination are employed [51]. Many variables have since been discovered to have a strong influences on the CVD process. These variables include the composition of the catalyst, the supporting substrate, the process temperature, and the process gases.

The transition metal nanoparticle catalysts used in the CVD have a major impact on the resulting CNTs. The metal must have sufficient carbon solubility at the growth temperatures to absorb the decomposed carbon atoms to begin the CNT growth process [48]. The two metals which exhibit the best CNT growth are Fe and Co [52], which have high carbon solubility at CVD temperatures. The catalyst-support interaction will also affect the catalyst reactivity[53]. In particular, catalyst supported on metal will have severely inhibited growth if bonding forms between the catalyst and metal support, which would prevent catalyst-carbon bonds. The catalyst particle size will also play a crucial role in the CVD process, as it will determine both the CNT growth rate and the resulting CNT diameters [48]. Supporting the catalyst metals on silica or alumina nanobeads prevents catalyst aggregation to maintain consistent particle sizes and provides a chemically known supporting material, which is very important as our catalyst sites will be supported on platinum contacts.

The chemical nature of the catalyst can also be improved by introducing a non-carbon-reactive metal compound to tune the main metal. For example, adding molybdenum to pure iron catalyst inhibits the formation of Fe_3C carbides which "poison" the growth of CNTs. These so called bimetal catalyst have been used to improve the CVD selectivity

of single wall CNT growth [54, 48]. Our CVD growths are carried out with a Fe-Mo-Co catalyst on silica nanobeads, to preferentially grow a high number of small single wall CNTs.

The CVD process temperature will determine the various reaction rates in the growth. If the temperature is too low the chemical decomposition of precursor at the catalyst will be slow or completely absent and only low density, short CNTs will form. At high temperatures the thermal decomposition of the precursor begins to occur, causing amorphous carbon to be deposited on the CNTs and over the catalyst free regions of the devices.

The volume and balance of gases in the CVD process will control the decomposition and absorption of the carbon atoms at the catalyst. The desired gas behaviour is for the hydrocarbon gas to decompose completely, and for the carbon atom to absorb into the catalyst while the non-carbon gases flow out of the CVD chamber. This requires the carbon to be decomposed at the correct rate. If the carbon concentration is too high, the carbon radicals will not all bond with the metal catalyst but will instead combine with each other and form amorphous carbon [48]. If the carbon concentration is too low, the lack of decomposition will result in very short or no CNTs, which will not permit suspended growth as we desire. The decomposition rate of the hydrocarbons can be controlled by the hydrogen levels present during growth [55] to achieve a clean growth of long CNTs.

3.3.2 CVD Process for Our Devices

As mentioned above, the catalyst solution we use for CVD growth combines the highly carbon soluble Fe and Co, with Mo to selectively grow single wall CNTs. The catalyst concentration and deposition techniques, as well as the CVD process settings have been iterated towards high quality suspended CNTs. For individual high quality suspended CNT devices we desire very low defect CNTs, grown with a moderate density, and we want to avoid having a large number of short, random tubes growing near the catalyst site.

Catalyst deposition

The catalyst is patterned using a masked solution deposition, in which the catalyst material is suspended in liquid and dispensed onto a masked sample, followed by drying and liftoff of the mask. Acetate particles containing the desired catalyst metals are combined

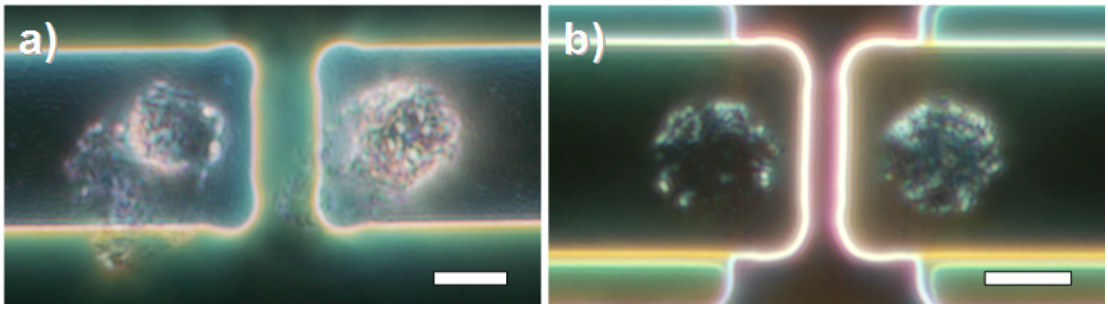

Figure 3.4: Dark field optical images of CNT catalyst material deposited using **a)** monolayer and **b)** bilayer photolithography. Scale bars are 5 μm.

with silica nanobeads as the catalyst support (full catalyst recipe in appendix B). The acetate structure is broken down in a repeatable manner during CVD growth leaving small metal particles as catalyst. The catalyst materials are sonicated into the suspension liquid, with liquids being either distilled water, isopropanol, or acetone. It was found that the silica particles do not disperse well in water and produce very uneven/missing catalyst islands. The acetone solvent had very good dispersion, but was incompatible with the photolithography resist we eventually used and would leave large catalyst deposits in undesired locations. The isopropanol had reasonable dispersion of the catalyst material and minimal resist dissolving, and thus was the liquid used for the growths discussed below.

As mentioned, the catalyst material is dispensed onto a masked sample. Initially, a single layer photolithography process was used, however this sometimes resulted in "smeared" catalyst islands as shown in figure 3.4a that would create CNT films growing over the contact edges. This was attributed to catalyst material building along the wall of the photoresist island pattern, and then collapsing during liftoff. Thus, a bilayer photoresist was used, as with metal deposition, to prevent a continuous catalyst film up the sidewall, resulting in repeatably clean catalyst islands as shown in figure 3.4b.

Ethanol CVD

The initial growth attempts on these devices were carried out in a 2" CVD chamber using ethanol precursor (the CVD recipe is given in appendix B). Figure 3.5a shows an example Raman spectrum measured on CNT films obtained from this growth. The radial breathing mode (RBM) peaks at 100 cm^{-1} to 300 cm^{-1} and the G peak at $\sim$ 1600cm^{-1} indicate

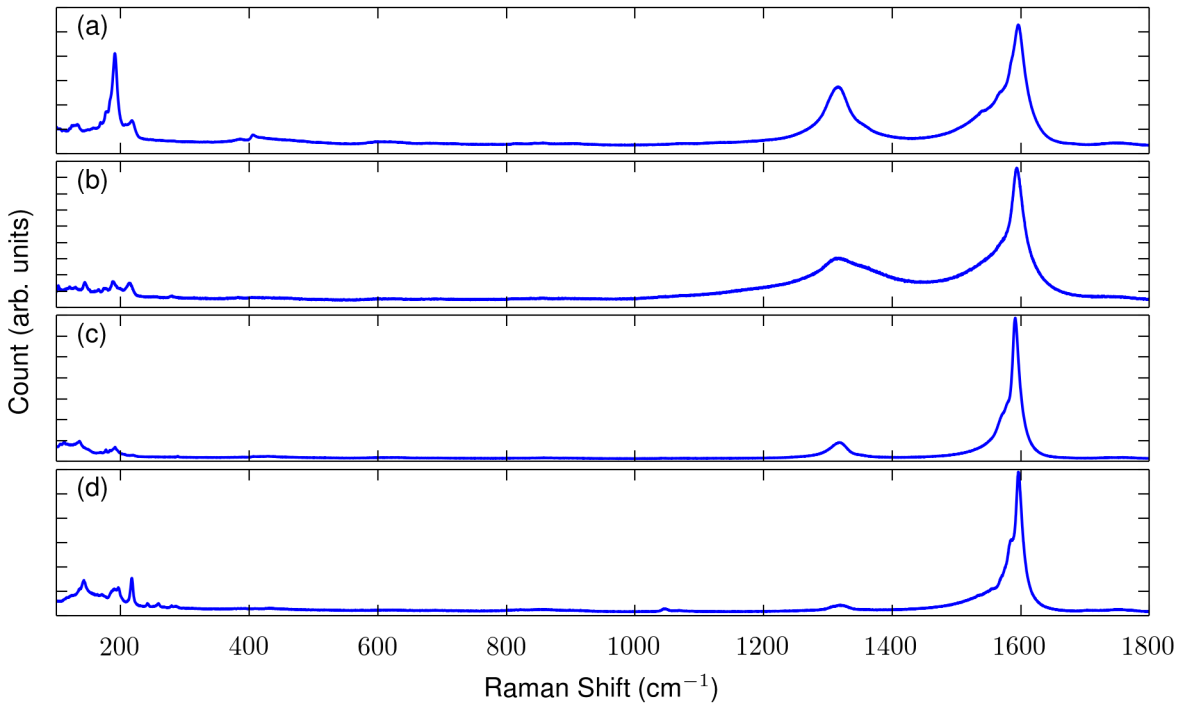

Figure 3.5: Raman spectra of CNT catalyst regions on platinum resulting from **a)** ethanol precursor CVD, **b)** ethylene precursor CVD, **c)** early methane precursor CVD recipe, and **d)** final methane precursor CVD recipe.

the presence of CNTs, however the large D peak at $\sim 1320\text{cm}^{-1}$ indicates a large number of defects in these CNTs [56]. Adjustments of process temperature, catalyst composition, and gas flows were not able to significantly reduce this defect density.

Ethylene CVD

With the goal of reducing the defect density in the CNTs, we switched to an ethylene precursor for the CVD in a 1" CVD chamber (full recipe in appendix B). Figure 3.5b shows a typical Raman spectrum from these growths. While CNTs are again present, the broad D peak indicates the presence of amorphous carbon [57]. This was confirmed visually as dark deposits in many sample regions. The amorphous carbon was attributed

to excess carbon decomposition during the growth, necessitating a large reduction in the carbon balance.

Methane CVD

To reduce both the CNT defects and amorphous carbon deposition, a new methane CVD process was used. These growths are performed in a 1" CVD chamber using methane precursor.

The initial methane recipe was extracted from prior work by members of the Tang lab on patterned catalyst. Figure 3.5c shows an example Raman spectrum from these growths, showing a lack of amorphous carbon and an improvement in the CNT quality as evidenced by the greatly reduced D peak over the non-methane CVD processes. However, these CNTs were observed to be short ($\lesssim 5$ μm) and randomly oriented, making them unusable for suspended devices. The short CNT growth was attributed to a scarcity of decomposed carbon leading to growth termination, as a result of poor C-H ratio and volume.

The final CVD recipe was adapted from [51] to stimulate defect free growth of long nanotubes. It also allows for the possibility of gas flow alignment of sufficiently long CNTs. The gas flow settings are similar to reference [48], in which they used a similar catalyst and were growing suspended CNTs on Pt contacts, although their CVD chamber is a hot-load system with vacuum control. Our recipe is given in appendix B as methane recipe #2. Figure 3.5d shows a Raman spectrum from this growth, showing an even further reduced D peak intensity in comparison to the previous methane CVD. The lower defects and higher carbon concentration in the gas flows should permit longer, defect-free growths that will be capable of suspended growth over the trench between contacts.

To get an idea of the CNT diameters from our growths, figure 3.6 shows an expanded view of the RBM range of the Raman spectrum from figure 3.5d. The RBM frequency is proportional to the CNT diameter [58], where the relation can be expressed as

$$\omega_{RBM} = \frac{c_1}{d} + c_2 \tag{3.1}$$

with $c_1 = 215 - 260$ cm^{-1}nm and $c_2 = 0 - 20$ cm^{-1}. Using this equation, the strong peak at 218 cm^{-1} is estimated to indicate $\approx 1 - 1.3$ nm diameter CNTs. The smaller peaks at 240 cm^{-1} and 260 cm^{-1} could represent CNT diameters as small as 0.8 nm. It should be

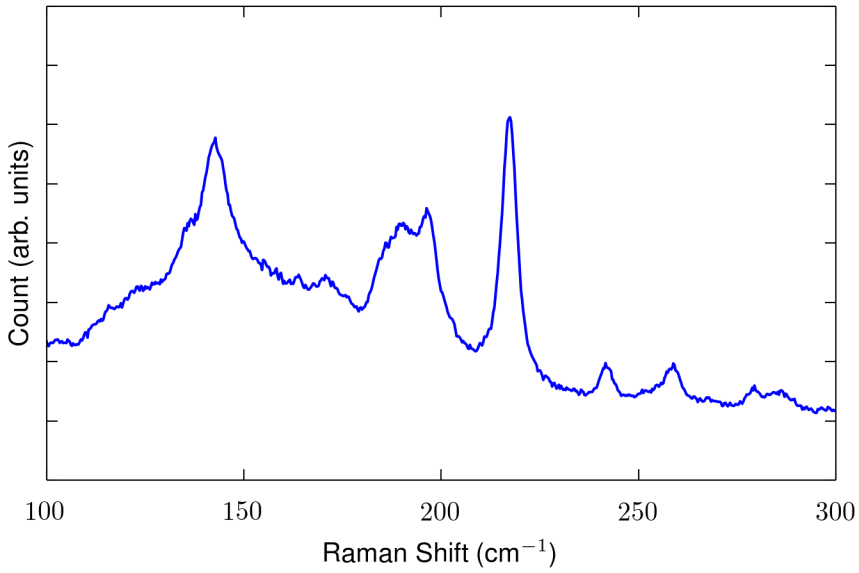

Figure 3.6: The radial breathing mode range of the Raman spectrum of a CNT device grown using the final methane CVD recipe.

noted that these spectra were taken over a catalyst dense region and thus include both long tubes that would grow away from the catalyst and short random tubes between catalyst. Therefore, the final diameter distribution of long tubes is not necessarily the same.

Finally, figure 3.7 shows atomic force microscopy (AFM) images of CNTs grown using the final methane CVD recipe. These devices were test devices consisting of Ti/Pt contacts on SiO_2 with no trenches or fine gate patterns. For each device the gas flow was in the direction from drain to source contact. Figure 3.7a shows an individual long, straight CNT bridging the contacts, with the CNT direction aligned with the gas flow. Figure 3.7b and 3.7c both show a CNT bridging the gap as a long straight tube within $\pm 15^\circ$ of the gas flow, and that same CNT curving back on the bottom Pt contact and recrossing the gap as a curved tube (recrossing identified in AFM phase data and confirmed by equal CNT height measurements). Figure 3.7c also shows an extra CNT looping off one Pt contact and quickly returning to it. The measured CNT diameters are 2.4 nm for (a), 1.4 nm for (b), and 1.0 nm and 1.1 nm for (c).

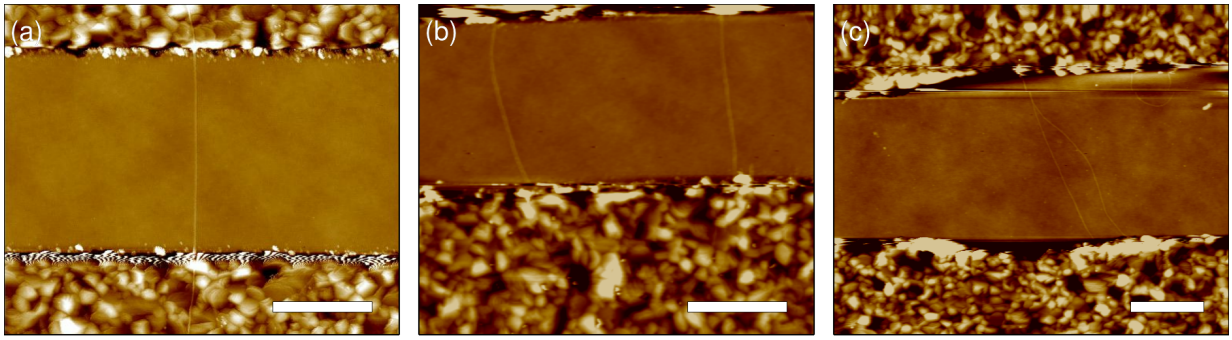

Figure 3.7: AFM height measurements for three select CNT test devices, grown using the final methane CVD process. The colorscale (black-to-white) is 100 nm for **a**, 20 nm for **b**, and 15 nm for **c**. All scale bars are 0.5 μm. All images were taken using tapping mode AFM, and have been horizontally line flattened via the AFM analysis software such that each horizontal line has a zero average height.

3.4 Preliminary Device Characterization

302 potential devices, created with the fabrication process detailed in section 3.1 and the last methane CVD recipe, were tested using a room temperature probe station. While 33 of these devices showed some connection between source and drain, most of these devices also had connections from the source and drain to the gate. This could indicate either extra CNTs contacting the gate directly from the source and/or drain, or it could indicate the CNT between the source and drain had sagged into the trench. The former case was identified in one of these devices, in which a metallic CNT contact was measured between the source and gate, while a semiconducting contact was observed between the drain and gate.

Five potentially suspended devices were identified from the 33 above device, which had connection between source and drain and no source-drain connection to the gate. The room temperature gate-dependence of the source-drain current was used to label these tubes as semiconducting or quasi-metallic as described below. Figure 3.8 shows the gate-dependence measurements of three of these devices. The semiconducting CNTs are pinched off (I = 0) with $V_g \sim 1$V, while the quasi-metallic CNT shows only weak gate dependence at these gate voltages. Using this criteria, three of the five suspended CNTs were identified as semiconducting, with room temperature source-drain resistances ranging from 480kΩ

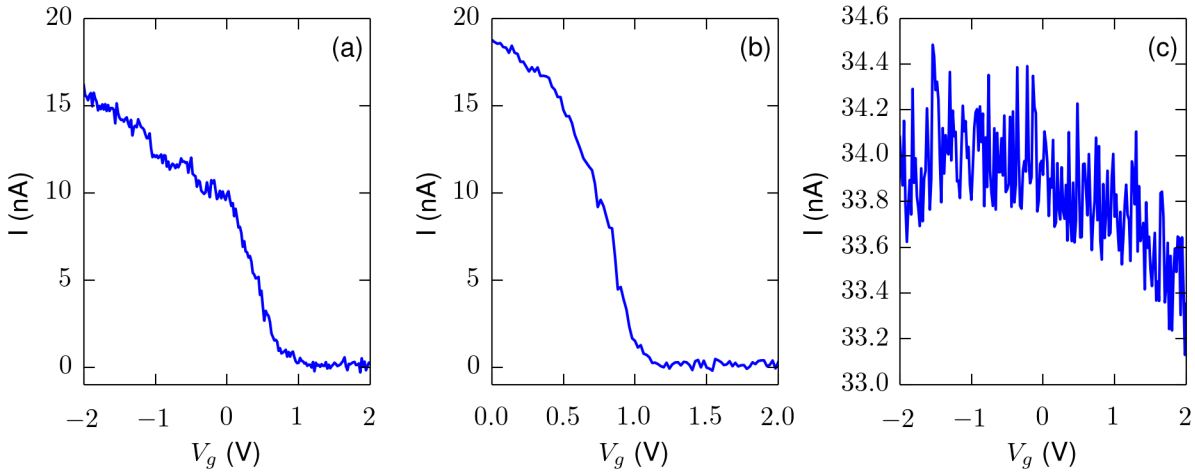

Figure 3.8: Room temperature gate dependence measurements of **a**,**b)** semiconducting CNTs and **c)** a quasi-metallic CNT. All measurements were taken with 10 mV bias voltage. Note there is a $\approx 250\text{k}\Omega$ line resistance in this measurement set-up.

to 720kΩ, measured at 10mV bias voltage. The remaining two devices, identified as small bandgap CNTs, had room temperature source-drain resistances of $R \approx 50\text{k}\Omega$.

It is expected that the semiconducting CNTs would have very low conductance at cryogenic temperatures as a result of the high Schottky barriers ($\gtrsim$ 0.1 eV).This was confirmed by attempts at DC transport measurements at 1.2K having no observable signal in semiconducting CNTs. Low temperature transport measurements of one of the small bandgap CNT devices are presented below.

In addition to the potentially suspended devices, a set of non-suspended field effect transistor (FET) devices were fabricated. These used the same source-drain contacts as the suspended devices, but no trench or gate patterning was performed and a doped silicon wafer was used to act as the back gate. In these devices, the CNT is expected to lay across the SiO_2 substrate between the contacts. Figure 3.9a shows the conductance of a small-bandgap CNT FET device measured at 1.2K. The main observation from this device is that while measurable hole conductance ($V_g < 0$) is present, no electron conductance ($V_g > 0$) can be observed, which was observed even when increasing current preamplifier sensitivity. The suppression of electron transport in CNT FETs has been attributed by other researchers to interactions with particles absorbed on the supporting substrate [59].

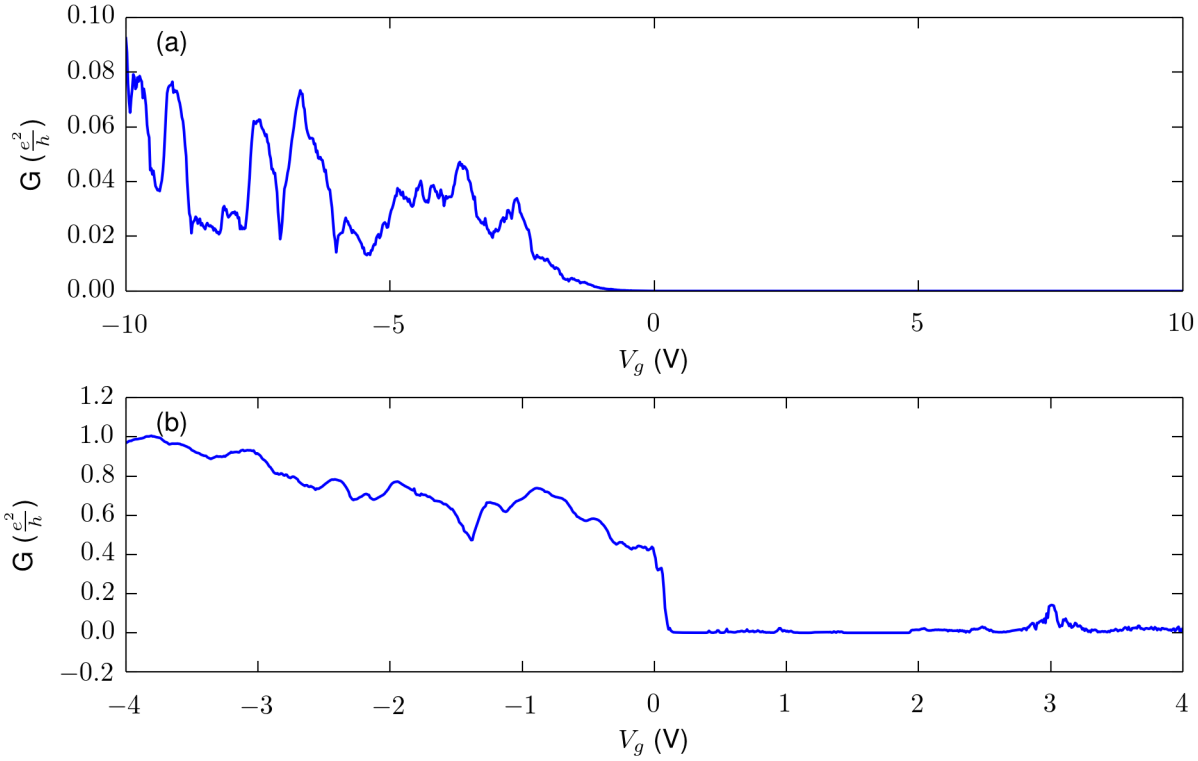

Figure 3.9: Gate dependence of CNT FET conductance at 1.2K in **a)** a non-suspended CNT on SiO_2 (measured at $V_{sd} = 10$ mV), and **b)** an apparently suspended CNT (measured at $V_{sd} = 5$ mV). Measurements were performed in a Janis 6T/2T-SVM-SV-20 pumped 4He cryostat with the sample in vacuum.

Figure 3.9b shows a low bias gate sweep of a potentially suspended small-bandgap CNT device at 1.2K. In this device, the electron transport was observed, which could be attributed to a lack of interactions with SiO_2 and surface absorbents. Note that the electron conductance is still much lower than the hole conductance, as expected for CNT-Pt contacts which are more transparent to holes [20]. Note that no current or thermal annealing of either of these devices was performed, with each device having a maximum applied bias voltage of 20 mV while under vacuum.

Figure 3.10 shows the conductance, $G = \frac{\partial I}{\partial V_{sd}}$ for the suspended small-bandgap CNT device, measured at 1.2K. The first observation is the high conductance in hole transport as noted previously. We further note that the maximum magnitude of conductance in the hole transport reaches $\sim \frac{2e^2}{h}$. Similar CNT devices have typically reached hole conductance of $\sim \frac{e^2}{h}$ or less [60, 61]. This high conductance could be an indication that we have multiple conduction channels, such as multiple CNTs, which will be discussed further below.

As described in section 2.1.3, at these temperatures we expect single electron tunneling to describe electron transport in CNTs, resulting in Coulomb diamonds in the conductance. Based on the device geometry, a quantum dot forming between the contacts should have a Coulomb diamond with $\sim$ 10 mV gate voltage width and $U_c \approx 2 - 5$ meV. The small Coulomb diamonds are observed as expected, however there are additional, much larger diamond patterns affecting the small diamonds. Within these larger diamonds the small features are non-closing, indicating that the main quantum dot in the CNT is in series with other features [62, 63].

Figure 3.11 shows a finer gate voltage range measurement of the same device. In addition to the non-closing diamond pattern noted above, we observe a bright and separate diamond pattern overlayed. The apparent independence of the two patterns provides further indication that there are parallel conduction channels in this device.

Figure 3.12 shows the conductance for a small gate voltage range far into the electron transport regime, at a point where the large diamond features have closed. From the Coulomb peak spacing at zero bias we calculate a gate capacitance value of $C_g \approx e/\Delta V_g =$ 14.6 aF, where we have neglected electron confinement energies, as ΔE is approximately $0.2 - 0.4$meV $\sim k_B T$ for this length of CNT quantum dot [20]. The Coulomb diamond edge slopes allow us to calculate the source and drain capacitances [26], $C_s \approx 24.5$ aF and $C_d \approx 23.1$ aF, respectively. The quantum dot charging energy is $U_c \approx 2.58$ meV. Using equation (2.3) and typical parameters expected for these devices, $h = 200$ nm, $d = 1.5$ nm

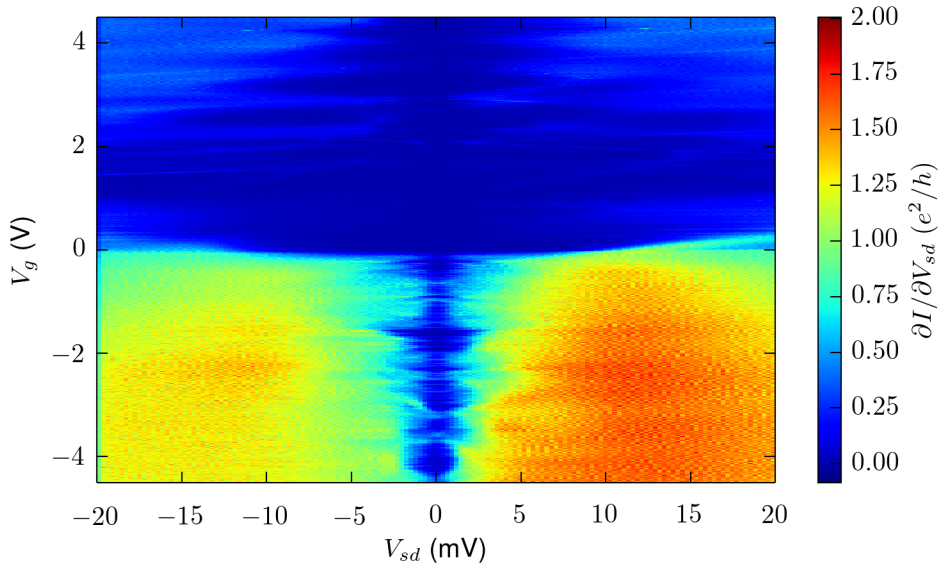

Figure 3.10: The conductance $\frac{\partial I}{\partial V_{sd}}$, in units e^2/h, as a function of V_g and V_{sd} for the CNT device from figure 3.9b, measured at 1.2K.

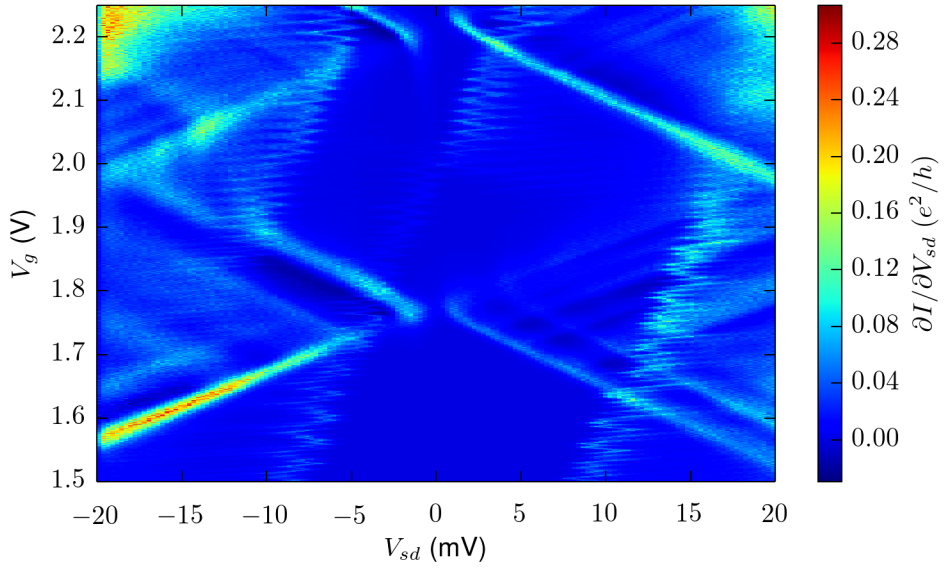

Figure 3.11: The conductance $\frac{\partial I}{\partial V_{sd}}$, in units e^2/h, as a function of V_g and V_{sd} for electron transport in the CNT device from figure 3.10, at 1.2K.

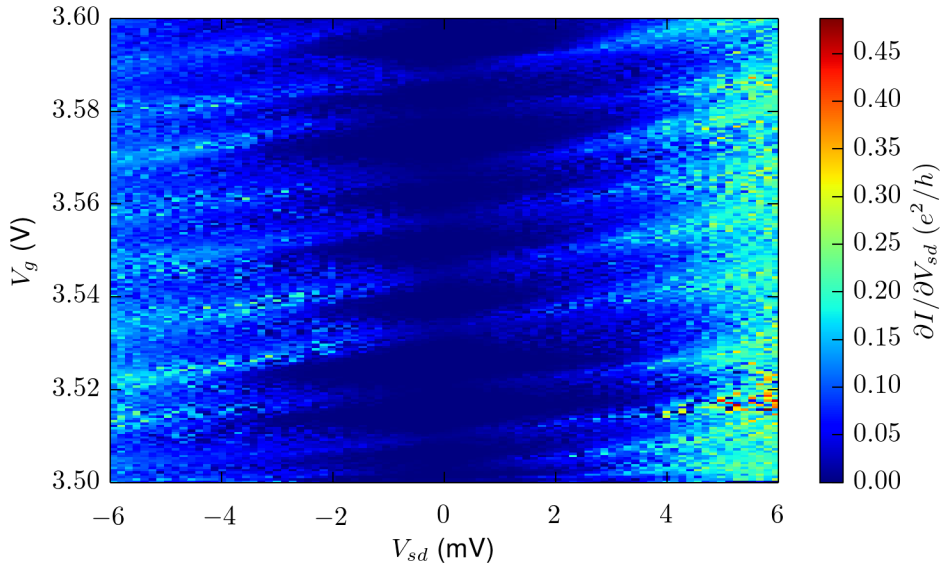

Figure 3.12: The conductance $\frac{\partial I}{\partial V_{sd}}$, in units e^2/h, far into the electron transport regime of the CNT device from figure 3.10, showing Coluomb diamonds of short period that correspond to a spatially large dot, consistent with the size of the entire CNT channel.

and $L = 1.5$ μm, we calculate a theoretical capacitance of 14.9 aF, in close agreement with the measured value, indicating that these small-period diamonds result from a dot along the entire CNT formed by tunnel barriers near the source and drain contacts.

Given that we are in the single electron tunneling regime ($k_BT \ll U_c$), the electron tunneling rates can be estimated from the Coulomb peak amplitudes [64]. If we approximate equal tunneling rates for both contacts ($\Gamma_R = \Gamma_L \equiv \Gamma$), the Coulomb peak height at zero bias has a simple analytic expression in two limiting cases. When $\Delta E \ll k_BT$ the tunnel rate can be expressed as [11],

$$\Gamma = 2\Delta E G_{peak}/e^2 \tag{3.2}$$

where G_{peak} is the zero bias conductance peak amplitude. When $\Delta E \gg k_BT$,

$$\Gamma = 8k_BTG_{peak}/e^2 \tag{3.3}$$

As noted above, $\Delta E \approx 0.2 - 0.4\text{meV} = 2.3 - 4.6$ K $\sim T$, and thus we are between these limits. Nevertheless, the tunnel rate will be in the range between the values given

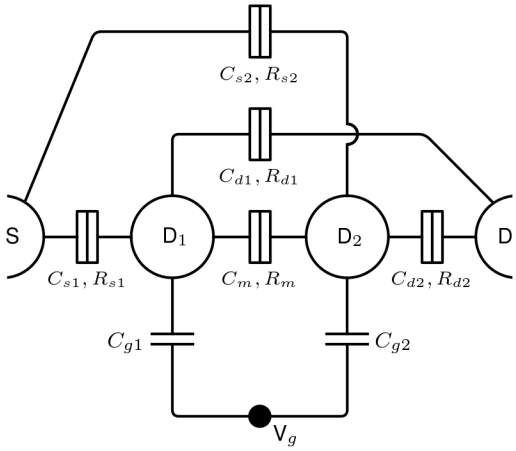

Figure 3.13: Circuit diagram of an arbitrarily connected double dot system with a single gate electrode. The gate is capacitively coupled to each dot. The dots are connected to each other and the source and drain reservoirs through tunnel junctions, which are effectively a parallel resistor and capacitor. Based on [65].

by the above equations [64]. Extracting $G_{peak} = 0.016e^2/h$ from fitting of the zero bias conductance peaks (see appendix C), equation (3.2) gives $\Gamma = 1.5$ GHz and equation (3.3) gives $\Gamma = 4.3$ GHz using $T = 1.6$ K as extracted from the same fitting. This tunnelling rate is roughly an order of magnitude smaller than has been reported for similar devices [60, 11], which could be a result of the sequential quantum dots that cause the non-closing diamonds above.

3.4.1 Conductance fitting

To understand the source of the non-closing Coulomb diamond features in figure 3.11, a simple model was created to estimate the conductance through arbitrarily connected double quantum dot system controlled by a single gate electrode. The circuit diagram of this model is shown in figure 3.13. The conductance is determined as a function of gate voltage and bias by solving for the steady state tunnel rates through all barriers and calculating the resulting current.

The chemical potentials of the source and drain are $\mu_s = eV_s$ and $\mu_d = eV_d$, respectively. The chemical potentials of each dot are calculated with the constant interaction model, neglecting orbital energies [65]

$$\mu_k(N_1, N_2) = \left(N_k - \frac{1}{2}\right) E_{Ck} + N_{\bar{k}} E_m - \frac{1}{|e|}\left(C_{gk} V_g E_{Ck} + V_{g\bar{k}} V_g E_m\right), \qquad k = 1, 2 \quad (3.4)$$

where $\bar{k} = 2 - k$, N_k is the number of electrons on dot k, and the charging and coupling energies are

$$E_{Ck} = \frac{e^2}{C_k\left(1 - \frac{C_m^2}{C_1 C_2}\right)}, E_m = \frac{e^2}{C_m\left(\frac{C_1 C_2}{C_m^2} - 1\right)}$$

with $C_k = C_{sk} + C_{dk} + C_{gk} + C_m$.

The tunneling rates between all possible states of the dots and leads are then calculated as

$$\Gamma_{\alpha,\beta}(N_1, N_2) = \frac{K_\alpha - K_\beta}{e^2 R_{\alpha,\beta}\left(1 - \exp\left(-\frac{K_\alpha - K_\beta}{k_B T}\right)\right)} \quad (3.5)$$

where $R_{\alpha,\beta}$ is the resistance of the tunnel coupling between the two elements, $K_\alpha = \mu_\alpha(N_1^\alpha, N_2^\alpha)$ is the chemical potential before the tunneling of the element the electron is tunneling from, and $K_\beta = \mu_\beta(N_1^\beta, N_2^\beta)$ is the chemical potential after tunneling of the element the electron tunnels to.

The master equation for the electron occupation number of the double dot system is then [63]

$$\begin{aligned}
\dot{\rho}_{N_1,N_2} = -\Gamma_{out}(N_1, N_2)\rho_{N_1,N_2} &+ (\Gamma_{s1}(N_1 - 1, N_2) + \Gamma_{d1}(N_1 - 1, N_2))\rho_{N_1-1,N_2} \\
&+ (\Gamma_{s2}(N_1, N_2 - 1) + \Gamma_{d2}(N_1, N_2 - 1))\rho_{N_1,N_2-1} \\
&+ (\Gamma_{1s}(N_1 + 1, N_2) + \Gamma_{1d}(N_1 + 1, N_2))\rho_{N_1+1,N_2} \\
&+ (\Gamma_{2s}(N_1, N_2 + 1) + \Gamma_{2d}(N_1, N_2 + 1))\rho_{N_1,N_2+1} \\
+\Gamma_{12}(N_1 + 1, N_2 - 1)\rho_{N_1+1,N_2-1} &+ \Gamma_{21}(N_1 - 1, N_2 + 1)\rho_{N_1-1,N_2+1}
\end{aligned} \quad (3.6)$$

where Γ_{out} is the sum of all tunneling rates with electron numbers (N_1, N_2). To determine the current through the double dot system, the steady state of equation 3.6 is solved numerically. The current is then calculated as the current through the source [63]

$$I = e \sum_{N_1,N_2} \left(\Gamma_{s1}(N_1, N_2) + \Gamma_{s2}(N_1, N_2) - \Gamma_{1s}(N_1, N_2) - \Gamma_{2s}(N_1, N_2)\right) \rho_{N_1,N_2} \quad (3.7)$$

To attempt to match conductance measured in the CNT device, the capacitances of the system were extracted as was done for figure 3.12, for both the small diamond and large diamond features. The interdot capacitance, C_m, was estimated at the order of magnitude of the source-dot capacitance and was adjusted in finding a fit of the data. The tunnel resistances were estimated starting from the above calculations and adjusted to fit. The best fit results are shown in figure 3.14b, with the relevant segment of the conductance shown in figure 3.14a for convenience (the data is equivalent to figure 3.11). The fit shown uses temperature of 1.2K, capacitance values of $C_{s1} = 44$ aF, $C_{d1} = 9.9$ aF, $C_{g1} = 10$ aF, $C_{s2} = 0.25$ aF, $C_{d2} = 21$ aF, $C_{g2} = 0.358$ aF, $C_m = 2$ aF and tunnel conductance ratios ($G = 1/R$) of $G_{s1} : G_{d1} : G_{s2} : G_{d2} : G_m = 20 : 0.01 : 0 : 3 : 12$. Note that the experimental conductance through the system is higher for positive bias, which could be due to bias-dependent tunnel barriers [44] which are not accounted for in our simple model.

Of particular interest from the fitting values is that one dot is strongly connected and coupled to the drain and only weakly capacitively coupled to the gate and source, while the other dot is connected as expected for a CNT bridging the source-drain but with a much weaker drain connection. This situation can be explained as a physical gap or bump near the edge of the drain contact causing both a mechanical kink in the CNT and a weak connection to the primary dot. The mechanical kink would act as a tunnel barrier between the dots within the CNT by either opening a local bandgap [66], or acting directly as a tunnel barrier [67, 68, 69]. The gap or bump in the drain contact could be a result of large grains forming in the Ti/Pt contacts, which can be seen in figure 3.7.

3.5 Discussion

The capacitance estimates from the fine Coulomb diamonds suggest that we have a CNT forming a quantum dot of the size we expect, in the location we expect. However, the conductance measurements also include unexpected and undesirable features. The parallel Coulomb diamonds and high hole conductance indicate that we may have multiple CNT channels. Additionally, the large period, non-closing Coulomb diamond patterns indicate at that at least one additional dot is forming in series with the primary island. Fitting to this non-closing pattern suggests that this confinement is due to a feature at the drain contact, potentially from mechanical kinking and poor connection due to the grainy nature of the Ti/Pt contacts after CVD growth.

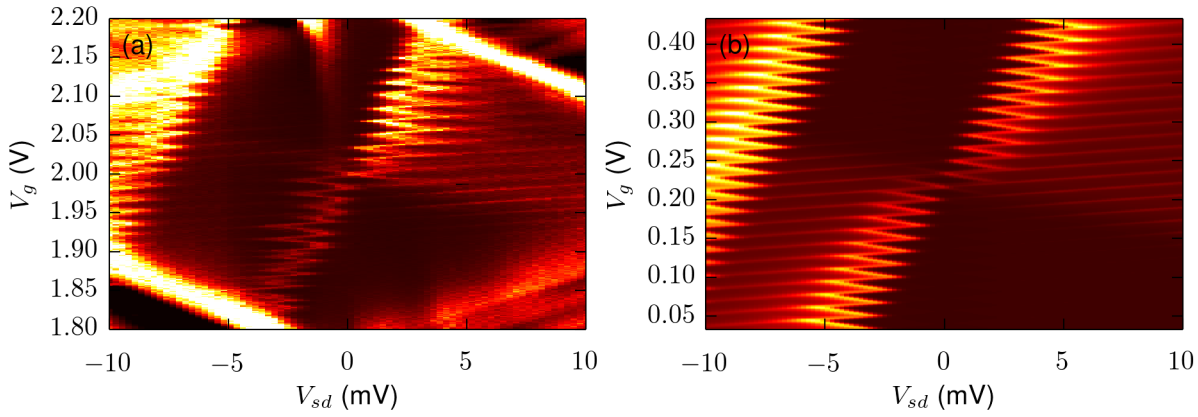

Figure 3.14: **a)** The measured conductance of the CNT device from figure 3.10 at 1.2K. **b)** Numerically calculated conductance using the arbitrarily coupled double dot model and parameters described in the text. The fitted model suggests that in addition to the dot formed by the entire CNT channel, there is an additional small dot in series located near the drain electrode.

3.5.1 Future Fabrication Improvements

To reduce the large grains observed in the Ti/Pt contacts after CVD growth of the CNTs, a new metal stack could be employed. While the Ti/Pt stack was chosen to endure the CVD process and be compatible with the available QNCFab facility, the grain size could be causing both the above kinking issues and long CNT growth inhibition. It has been found in similar processes that a W/Pt metal stack could greatly reduce the graining effect [70, 61] and result in smoother contacts after CVD growth.

The low yield of suspended CNTs with usable gates could be attributed to low probability of growing suspended CNTs and/or a high number of extra CNTs growing between the source/drain contacts and the gate. The first problem can be addressed by reducing the source-drain separation, and by decreasing the trench aspect ratio by deepening the trench. While a deeper trench is compatible with the current device process, the source-drain separation is currently at the minimum line spacing possible with PMGI-S1805 bilayer photolithography before the bilayer collapses. Finer line spacing can be achieved by employing surface-modification resist processing in which $\sim$ 100nm undercuts are created in single layer photoresist by chemically treating the resist surface [71, 61]. Once higher

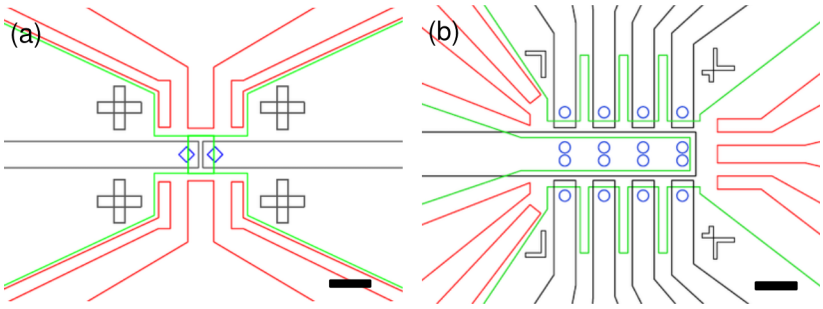

Figure 3.15: **a)** The current photomask design, featuring one device per region. **b)** The updated photomask design, featuring eight devices per equal-sized region. Scale bars are 20 μm.

suspension yields are realized, the process temperature and catalyst densities can be reduced to decrease the probability of CNTs growing off the contacts into the gates, and reduce the possibility of too many CNTs bridging the contacts.

Even with design improvements to get more suspended CNTs, the suspension yield of this fabrication is not expected to exceed $\sim$ 5%, and thus processing a large number of devices will be important to obtain a useful number of devices. While we currently make use of wafer-scale processing for the majority of the fabrication, both the electron beam lithography and CVD chamber require smaller processing and samples, and as a result the device fabrication process remains slow. The device throughput can be improved by increasing the device density, allowing the smaller processing to handle a larger number of devices. Figure 3.15b shows a new photomask design which increases the device density by a factor of 8 over the current photomasks shown in figure 3.15a, while still using the same fabrication steps and full wafer processing.

Finally, while our CVD process is capable of creating $\approx$ 1 nm diameter CNTs, as evidenced by the ω_{RBM} data, it also creates a large fraction of larger diameter CNTs. The force sensitivity of our ultimate device will depend on the spring constant of the CNT, and will be greatly improved for smaller diameter CNTs. To decrease the average CNT diameter, and reduce the diameter distribution, we could make use of chemically well-defined catalyst particles [72, 73, 74], or a different bimetal catalyst such as Fe-Ru that promotes smaller CNT growth [48]. The chemically defined catalysts have exact numbers of active catalyst metal atoms in a supporting structure that is broken down during the

CVD process, leaving a metal island of known size. The Fe-Ru bimetal slows the carbon decomposition rate of the catalyst metals, which then favors growth from smaller catalyst particles, at the cost of growth density. In reference [48], Fe-Mo catalyst resulted in a 1.6 nm average CNT diameter, while the equivalent process using Fe-Ru resulted in 1.1 nm average CNT diameter. We would expect a similar shift in our CVD-grown CNT diameters.

Chapter 4

Modelling magnetic moment sensing with suspended carbon nanotubes

This chapter presents the magnetic force sensor concept, then derives and uses numerical simulations to assess the sensor performance. Much of the work presented in this chapter has been published in:

> Willick K, Haapamaki C, Baugh J. Sensitive magnetic force detection with a carbon nanotube resonator. J Appl Phys. **115** 114501 (2014)

4.1 Proposed Sensing Technique

To make use of a CNT resonator for magnetic moment sensing, the magnetic moment of interest needs to be coupled to an observable effect in the resonator. By making use of the resonator readout methods in section 2.4, this coupling can be achieved by affecting the resonant frequency of the CNT resonator. To generate a magnetic moment dependency in the resonant frequency, we note the impact of applied forces in section 2.3, and aim to generate a perpendicular force on the CNT that depends on the nanomagnet's magnetic moment. By grafting the nanomagnet to the CNT, the required magnetic moment dependent force can be accomplished by generating this force on the nanomagnet.

Reference [6] made use of a CNT resonator for studying a SMM through a related mechanism. In that case, the SMM of interest had a uniaxial magnetic anisotropy that

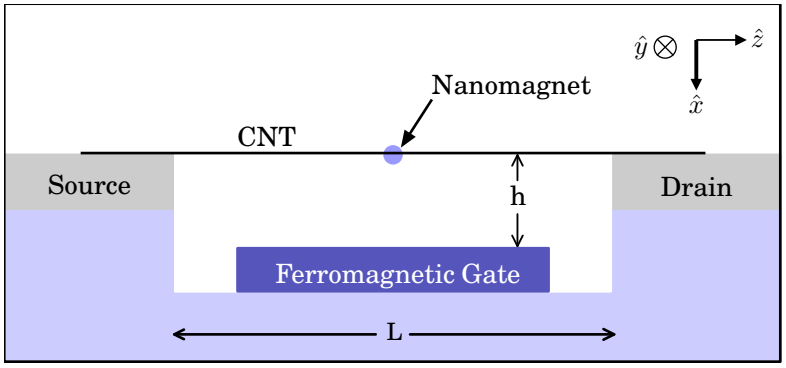

Figure 4.1: Schematic of the proposed device, showing the ferromagnetic gate combined with a CNT resonator and attached nanomagnet.

could be engineered to align perpendicular to the CNT axis via control of the particular SMM ligand structure. In the presence of an external magnetic field applied along the CNT axis, a torque would be exerted on the anisotropic SMM moment, and this torque would impact the resonance frequency of the CNT. This measurement technique requires an anisotropic nanomagnet and finite grafting length for the torque to act upon. The technique proposed in this chapter seeks to reduce these restrictions and greatly improve sensitivity, to allow further studies of nanomagnetic behavior over a broader range of nanomagnets.

To achieve a strong nanomagnet-CNT coupling and reduce restrictions on the nanomagnet and grafting, we want to generate a force on any nanomagnet, that will act perpendicular to the CNT axis and depend on the magnetic moment. This can be achieved by having a gradient in the magnetic field at the nanomagnet position. To achieve the required magnetic field gradient, we can fabricate a localized magnetic structure using the same nanofabrication used to create typical suspended CNT devices, as described in chapter 3. In the proposed device, shown in figure 4.1, the metallic gate of a locally gated suspended CNT is replaced with a ferromagnetic gate. When this gate is magnetized, it will produce a localized field. Due to the small size of this gate and the proximity of it to the CNT, there will be a strong gradient in this magnetic field at the nanomagnet position. As shown in the next section, this force will act in the field gradient direction, thus giving a magnetic moment dependent force acting perpendicular to the CNT axis.

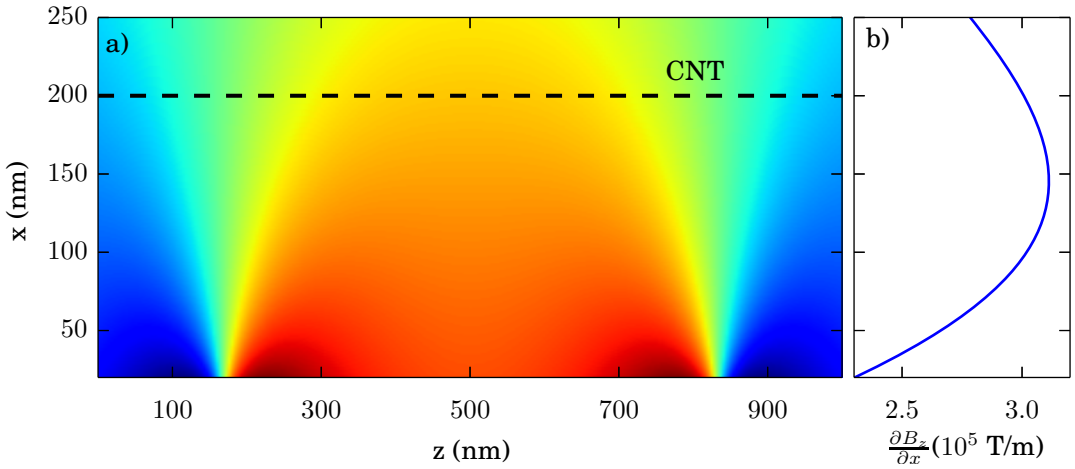

Figure 4.2: **a)** Magnetic field B_z along z generated by a 200 nm thick by 800 nm wide Cobalt gate at saturation magnetization, 10^6 A/m, with the nominal CNT location depicted. **b)** The field gradient $\frac{\partial B_z}{\partial x}$ at the center of the suspended CNT channel as a function of the distance from the gate.

4.2 Force on Nanomagnet

Figure 4.2a shows the z-component of the magnetic field generated by a 800 nm wide by 200 nm thick cobalt gate at saturation magnetization aligned along $\hat{z}$ [75, 76]. Figure 4.2b shows the derivative of this field component along the x-axis at the center of the CNT, the nominal nanomagnet location.

The energy of a magnetic moment in a magnetic field is given by

$$U = -\vec{m} \cdot \vec{B} \tag{4.1}$$

The force due to the field potential is then

$$F = -\nabla U \tag{4.2}$$
$$= \nabla\left(\vec{m}\cdot\vec{B}\right) \tag{4.3}$$
$$= \left(\left(\vec{m}\cdot\nabla\right)\vec{B} + \left(\vec{B}\cdot\nabla\right)\vec{m} + \vec{m}\times\left(\nabla\times\vec{B}\right) + \vec{B}\times\left(\nabla\times\vec{m}\right)\right) \tag{4.4}$$
$$= \left(\left(\vec{m}\cdot\nabla\right)\vec{B} + \vec{m}\times\left(\nabla\times\vec{B}\right)\right) \tag{4.5}$$
$$= \left(\left(m_x\frac{\partial}{\partial x} + m_y\frac{\partial}{\partial y} + m_z\frac{\partial}{\partial z}\right)\vec{B} + \vec{m}\times\left(\nabla\times\vec{B}\right)\right) \tag{4.6}$$

where (4.4) to (4.5) comes from $\vec{m}$ being independent of position

Continuing component-wise

$$F_x = \left(\left(m_x\frac{\partial B_x}{\partial x} + m_y\frac{\partial B_x}{\partial y} + m_z\frac{\partial B_x}{\partial z}\right) + m_y\left(\frac{\partial B_y}{\partial x} - \frac{\partial B_x}{\partial y}\right) - m_z\left(\frac{\partial B_x}{\partial z} - \frac{\partial B_z}{\partial x}\right)\right) \tag{4.7}$$
$$= \left(m_x\frac{\partial B_x}{\partial x} + m_y\frac{\partial B_y}{\partial x} + m_z\frac{\partial B_z}{\partial x}\right) \tag{4.8}$$

Similarly,

$$F_y = m_x\frac{\partial B_x}{\partial y} + m_y\frac{\partial B_y}{\partial y} + m_z\frac{\partial B_z}{\partial y} \tag{4.9}$$
$$F_z = m_x\frac{\partial B_x}{\partial z} + m_y\frac{\partial B_y}{\partial z} + m_z\frac{\partial B_z}{\partial z} \tag{4.10}$$

We can assume that the ferromagnet is much longer in the y-direction than our system dimensions, then $B_y = 0$ and $\frac{\partial \vec{B}}{\partial y} = 0$, giving that $F_y = 0$ for any SMM position. If we assume that the nanomagnet is approximately centered above the FM gate so that $\frac{\partial B_x}{\partial x} \approx 0$ and $\frac{\partial B_z}{\partial z} \approx 0$. Then the force on the SMM will be given by

$$F_x = m_z\frac{\partial B_z}{\partial x} \tag{4.11}$$
$$F_z = m_x\frac{\partial B_x}{\partial z} \tag{4.12}$$

The axial point force, F_z, will have negligible impact on the resonance of the CNT, and we will be primarily interested in magnetic moments aligned along $\hat{z}$ in which case $m_x = 0 \Rightarrow F_z = 0$. We will thus use the approximation that $F_{mag} = F_x = m_z\frac{\partial B_z}{\partial x}$.

4.3 Numerical Modelling

As mentioned in section 4.1, measuring the suspended CNT is achieved by monitoring its resonant frequencies. To understand how the perpendicular force on the nanomagnet, F_{mag}, will translate into resonant frequency signals, the suspended CNT is modelled as a Euler-Bernoulli beam and numerically evaluated. This Euler-Bernoulli model has shown good agreement with experimental data in similar CNT devices [77]. We model the electrostatic gate as a uniform force along the entire CNT length, and the nanomagnet force is described as a point force. The numerical calculation technique is motivated by a similar calculation in reference [78], in which the Euler-Bernoulli model was solved with only uniform forcing.

The governing equation for the Euler-Bernoulli model with these forces is

$$-EI\frac{\partial^4 x}{\partial z^4} + T\frac{\partial^2 x}{\partial z^2} + K_{elec} + F_{mag}\delta(z - z_0) - \eta\frac{\partial x}{\partial t} = \rho A\frac{\partial^2 x}{\partial t^2} \tag{4.13}$$

where E is the Young's modulus of the CNT, $I = \frac{\pi}{4}r^4$ is the moment of inertia, r is the CNT radius, x is the vertical displacement of the CNT from equilibrium, $T = T_0 + \frac{EA}{2L}\int_0^L \left(\frac{\partial x}{\partial z}\right)^2 dz$ is the tension in the CNT, T_0 is the residual tension at zero applied force as a result of fabrication, $K_{elec} = \frac{1}{2}c_g' V_g^2$ is the electrostatic force per unit length, $c_g' = \frac{2\pi\epsilon_0}{h(\ln(2h/r))^2}$ is the derivative of the CNT-gate capacitance per unit length with respect to x, z_0 is the nanomagnet position along the CNT, η is the damping factor per unit length, ρ is the CNT mass density, and A is the cross-sectional area of the CNT.

As mentioned in section 2.3, the CNT is tuned and driven with DC and AC gate voltages,

$$V_g = V_g^{dc} + V_g^{ac}\cos(\omega t) \tag{4.14}$$

with $V_g^{ac} \ll V_g^{dc}$. The resulting force on the CNT can then be decomposed

$$K_{elec} = \frac{1}{2}c_g'\left(V_g^{dc} + V_g^{ac}\cos(\omega t)\right)^2 \tag{4.15}$$

$$= \frac{1}{2}c_g'\left((V_g^{dc})^2 + V_g^{dc}V_g^{ac}\cos(\omega t) + (V_g^{ac})^2\cos^2(\omega t)\right) \tag{4.16}$$

$$\approx \frac{1}{2}c_g'\left((V_g^{dc})^2 + V_g^{dc}V_g^{ac}\cos(\omega t)\right) \tag{4.17}$$

The CNT displacement will have a similar decomposition $x(z,t) = u(z) + v(z,t)$, where the steady state response will be of the form $v(z,t) = v(z)\cos(\omega t + \phi)$, with phase ϕ depending

on resonator and driving conditions. Finally, the tension in the CNT will also have a large static component and an oscillatory component, which we approximate to first order as $T = T_{dc} + T_{ac}$,

$$T_{dc} = T_0 + \frac{EA}{2L}\int_0^L \left(\frac{\partial u}{\partial z}\right)^2 dz \tag{4.18}$$

$$T_{ac} = \left(\frac{EA}{L}\int_0^L \left(\frac{\partial u}{\partial z}\frac{\partial v}{\partial z}\right) dz\right) \tag{4.19}$$

where we have neglected the tension component proportional to $\left(\frac{\partial v}{\partial z}\right)^2$.

Substituting these decompositions into Equation (4.13) gives separate governing equations for the DC and first-order AC components of the CNT motion.

$$-EI\frac{\partial^4 u}{\partial z^4} + T_{DC}\frac{\partial^2 u}{\partial z^2} + K_{elec}^{dc} + F_{mag}\delta(z - z_0) = 0 \tag{4.20}$$

$$-EI\frac{\partial^4 v}{\partial z^4} + T_{DC}\frac{\partial^2 v}{\partial z^2} + T_{AC}\frac{\partial^2 u}{\partial z^2} + K_{elec}^{ac}\cos(\omega t) - \eta\frac{\partial v}{\partial t} = \rho A\frac{\partial^2 v}{\partial t^2} \tag{4.21}$$

To simplify notation, we can scale the parameters

$$z' = \frac{z}{L}, u' = \frac{u}{r}, v' = \frac{v}{r}, T'_{dc} = \frac{L^2 T_{dc}}{EI}, k' = \sqrt{T'_{dc}}, f'_{dc} = \frac{K_{elec}^{dc} L^4}{rEI}, f'_{ac} = \frac{K_{elec}^{ac} L^4}{rEI}$$

$$f'_{mag} = \frac{F_{mag} L^3}{rEI}, \lambda = \frac{1}{L^2}\sqrt{\frac{EI}{\rho A}}, \eta' = \frac{\eta L^4}{\lambda EI}, \omega' = \frac{\omega}{\lambda}, t' = t\lambda$$

The scaled DC and AC governing equations can then be written as

$$\frac{\partial^4 u'}{\partial z'^4} - T'_{dc}\frac{\partial^2 u'}{\partial z'^2} = f'_{dc} + f'_{mag}\delta(z' - z'_0) \tag{4.22}$$

$$\frac{\partial^2 v'}{\partial t'^2} - \eta'\frac{\partial v'}{\partial t'} + \frac{\partial^4 v'}{\partial z'^4} - T'_{dc}\frac{\partial^2 v'}{\partial z'^2} - T'_{ac}\frac{\partial^2 u'}{\partial z'^2} = f'_{ac}e^{i\omega' t'} \tag{4.23}$$

To solve Equation (4.22), T'_{dc} is taken as a constant, and doubly clamped boundary

conditions are applied ($u'(0) = \frac{\partial u'}{\partial z'}(0) = u'(1) = \frac{\partial u'}{\partial z'}(1) = 0$). The solution is then

$$u'(z') = \frac{f'_{dc}}{2k'^2}\left(\frac{\sinh(k')}{k'(\cosh(k')-1)}(\cosh(k'z')-1) - \frac{\sinh(k'z')}{k'} - (z'^2 - z')\right) + \frac{f'_{mag}}{k'^3\sigma_3}\left(\sigma_1\left(\sinh(k'z') - k'z'\right) + \sigma_2\left(\cosh(k'z')-1\right)\right) + \frac{f'_{mag}}{k'^3}\left(\sinh(k'(z'-z'_0)) - k'(z'-z'_0)\right)\mathrm{H}(z'-z'_0) \quad (4.24)$$

where $\mathrm{H}(z')$ is the Heaviside step function, and

$$\sigma_1 = \cosh(k') - \cosh(k'z'_0) + \cosh(k'(1-z'_0)) - k'(1-z'_0)\sinh(k') - 1$$
$$\sigma_2 = \sinh(k'z'_0) - \sinh(k') + \sinh(k'(1-z'_0)) + k'z'_0 + k'(1-z'_0)\cosh(k') - k'\cosh(k'(1-z'_0))$$
$$\sigma_3 = k'\sinh(k') - 2\cosh(k') + 2$$

Equation (4.24) is used in Equation (4.18) to solve for a new value of T'_{dc}. The new T'_{dc} is then substituted into Equation (4.24) again. This process is iterated until the T'_{dc} result stabilizes.

To determine the resonant frequencies, we decompose the AC motion, $v'(z')$, into eigenstates of (4.23),

$$v'(z',t') = \sum_n v'_n \xi'_n(z) e^{i\omega'_n t'} \quad (4.25)$$

where $\xi'_n(z)$ is the amplitude profile of the n^{th} eigenmode, which oscillates with frequency ω'_n. The decomposition can be inserted into Equation (4.23) to determine equations for $\xi'_n(z)$ and ω'_n. In general, T'_{ac} will couple ξ'_m to ξ'_n for $m \neq n$, making this difficult to solve. However, for high Q resonators and near resonance excitation, v'_m is very small for all $m \neq n$. Therefore, the mode coupling caused by T'_{ac} can be neglected, and we get

$$v'_n\left[\left(-\omega'^2 + i\eta'\omega'\right)\xi'_n(z') + \frac{\partial^4 \xi'_n}{\partial z'^4} - T'_{dc}\frac{\partial^2 \xi'_n}{\partial z'^2} - T'^n_{ac}\frac{\partial^2 u'}{\partial z'^2}\right] = f'_{ac} \quad (4.26)$$

where $T'^n_{ac} = 4\int_0^1 \frac{\partial u'}{\partial z'}\frac{\partial \xi'_n}{\partial z'}dz'$ is the amplitude of the oscillatory T'_{ac} for mode ξ'_n.

Noting that T'^n_{ac} is independent of v'_n, it can be treated as a constant, in which case (4.26) describes the amplitude response of a damped driven harmonic oscillator if we can write

$$\frac{\partial^4 \xi'_n}{\partial z'^4} - T'_{dc}\frac{\partial^2 \xi'_n}{\partial z'^2} - T'^n_{ac}\frac{\partial^2 u}{\partial z'^2} = \omega'^2_n \xi'_n \quad (4.27)$$

To identify resonant frequencies of the CNT resonator, we must find ω'_n which have solutions in Equation (4.27). The resonant mode shape ξ'_n must be solved piecewise, due to discontinuities introduced by the point force from the nanomagnet. The mode shape will have homogeneous components (with $T'^n_{ac} = 0$) and a particular solution for finite T'^n_{ac}.

Away from the discontinuity at $z' = z'_0$, the homogeneous solution is of the form

$$\xi'^h_n = A_1 \cos(k'_+ z') + A_2 \sin(k'_+ z') + A_3 \cosh(k'_- z') + A_4 \sinh(k'_- z') \tag{4.28}$$

where $k'_\pm = \frac{1}{\sqrt{2}}\sqrt{\sqrt{T'^2_{dc} + 4\omega'^2_n} \mp T'_{dc}}$. The particular solution is

$$\xi'^p_n = A_5 \frac{\partial^2 u'}{\partial z'^2} \tag{4.29}$$

To simplify computation for $z' > z'_0$, we substitute $(1 - z')$ for z' in the homogeneous solution. Thus, the full mode shape solution is

$$\xi'_n = \begin{cases} A_1 \cos(k'_+ z') + A_2 \sin(k'_+ z') + A_3 \cosh(k'_- z') + A_4 \sinh(k'_- z') + A_5 \dfrac{\partial^2 u'}{\partial z'^2} & \text{if } z' \le z'_0 \\ B_1 \cos(k'_+ (1 - z')) + B_2 \sin(k'_+ (1 - z')) + B_3 \cosh(k'_- (1 - z')) & \\ \qquad + B_4 \sinh(k'_- (1 - z')) + B_5 \dfrac{\partial^2 u'}{\partial z'^2} & \text{if } z' > z'_0 \end{cases} \tag{4.30}$$

To determine the coefficients, we make use of the doubly clamped boundary conditions, matching conditions at $z' = z'_0$ and Equation (4.27). The boundary conditions are

$$\begin{aligned} \xi'_n(0) = 0 &\implies A_1 + A_3 + A_5 \left.\frac{\partial^2 u'}{\partial z'^2}\right|_{z'=0} \\ \left.\frac{\partial \xi'_n}{\partial z'}\right|_{z'=0} = 0 &\implies k'_+ A_2 + k'_- A_4 + A_5 \left.\frac{\partial^3 u'}{\partial z'^3}\right|_{z'=0} \\ \xi'_n(1) = 0 &\implies B_1 + B_3 + B_5 \left.\frac{\partial^2 u'}{\partial z'^2}\right|_{z'=1} \\ \left.\frac{\partial \xi'_n}{\partial z'}\right|_{z'=1} = 0 &\implies -k'_+ B_2 - k'_- B_4 + B_5 \left.\frac{\partial^3 u'}{\partial z'^3}\right|_{z'=1} \end{aligned}$$

As the only force in Equation (4.23) is the uniform electric force, the AC modeshape and its derivatives will be continuous up to and including the third derivative, providing four

matching conditions. Finally, substituting Equation (4.30) into Equation (4.27), gives an independent equation for both $z' < z'_0$ and $z' > z'_0$,

$$\begin{aligned} T'^n_{ac} + \omega_n^2 A_5 &= 0 \\ T'^n_{ac} + \omega_n^2 B_5 &= 0 \\ \implies A_5 &= B_5 \end{aligned}$$

Thus the mode shape coefficients are given by the solutions to

$$\begin{bmatrix} 1 & 0 & 1 & 0 & 0 & 0 & 0 & 0 & \frac{\partial^2 u'}{\partial z'^2}\Big|_{z'=0} \\ 0 & k'_+ & 0 & k'_- & 0 & 0 & 0 & 0 & \frac{\partial^3 u'}{\partial z'^3}\Big|_{z'=0} \\ 0 & 0 & 0 & 0 & 1 & 0 & 1 & 0 & \frac{\partial^2 u'}{\partial z'^2}\Big|_{z'=1} \\ 0 & 0 & 0 & 0 & 0 & -k'_+ & 0 & -k_- & \frac{\partial^3 u'}{\partial z'^3}\Big|_{z'=1} \\ c & s & ch & sh & -c_- & -s_- & -ch_- & -sh_- & 0 \\ -k'_+ s & k'_+ c & k'_- sh & k'_- ch & -k'_+ s_- & k'_+ c_- & k'_- sh_- & k'_- ch_- & \Delta_3 \\ -k'^2_+ c & -k'^2_+ s & k'^2_- ch & k'^2_- sh & k'^2_+ c_- & k'^2_+ s_- & -k'^2_- ch_- & -k'^2_- sh_- & 0 \\ k'^3_+ s & -k'^3_+ c & k'^3_- sh & k'^3_- ch & k'^3_+ s_- & -k'^3_+ c_- & k'^3_- sh_- & k'^3_- ch_- & \Delta_5 \\ T'^{A_1}_{ac} & T'^{A_2}_{ac} & T'^{A_3}_{ac} & T'^{A_4}_{ac} & T'^{B_1}_{ac} & T'^{B_2}_{ac} & T'^{B_3}_{ac} & T'^{B_4}_{ac} & T'^{A_5}_{ac} + \omega'^2_n \end{bmatrix} \begin{bmatrix} A_1 \\ A_2 \\ A_3 \\ A_4 \\ B_1 \\ B_2 \\ B_3 \\ B_4 \\ A_5 \end{bmatrix} = \begin{bmatrix} 0 \\ 0 \\ 0 \\ 0 \\ 0 \\ 0 \\ 0 \\ 0 \\ 0 \end{bmatrix} \tag{4.31}$$

where the following notation was used

$$c \equiv \cos(k'_+ z'_0), s \equiv \sin(k'_+ z'_0), ch \equiv \cosh(k'_- z'_0), sh \equiv \sinh(k'_- z'_0)$$
$$c_- \equiv \cos(k'_+(1 - z'_0)), s_- \equiv \sin(k'_+(1 - z'_0)), ch_- \equiv \cosh(k'_-(1 - z'_0)), sh_- \equiv \sinh(k'_-(1 - z'_0))$$

$$\begin{aligned} \Delta_3 &= \frac{\partial^3 u'}{\partial z'^3}\Big|_{z'=z_0^-} - \frac{\partial^3 u'}{\partial z'^3}\Big|_{z'=z_0^+} \\ \Delta_5 &= \frac{\partial^5 u'}{\partial z'^5}\Big|_{z'=z_0^-} - \frac{\partial^5 u'}{\partial z'^5}\Big|_{z'=z_0^+} \end{aligned}$$

and ${T'}_{ac}^{X}$ is the component of ${T'}_{ac}^{n}$ with coefficient X,

$$
\begin{aligned}
{T'}_{ac}^{A_1} &= -4k'_+ \int_0^{z'_0} \frac{\partial u'}{\partial z'} \sin(k'_+ z')dz' \\
{T'}_{ac}^{A_2} &= 4k'_+ \int_0^{z'_0} \frac{\partial u'}{\partial z'} \cos(k'_+ z')dz' \\
{T'}_{ac}^{A_3} &= 4k'_- \int_0^{z'_0} \frac{\partial u'}{\partial z'} \sinh(k'_+ z')dz' \\
{T'}_{ac}^{A_4} &= 4k'_- \int_0^{z'_0} \frac{\partial u'}{\partial z'} \cosh(k'_+ z')dz' \\
{T'}_{ac}^{B_1} &= 4k'_+ \int_{z'_0}^{1} \frac{\partial u'}{\partial z'} \sin(k'_+ (1-z'))dz' \\
{T'}_{ac}^{B_2} &= -4k'_+ \int_{z'_0}^{1} \frac{\partial u'}{\partial z'} \cos(k'_+ (1-z'))dz' \\
{T'}_{ac}^{B_3} &= -4k'_- \int_{z'_0}^{1} \frac{\partial u'}{\partial z'} \sinh(k'_+ (1-z'))dz' \\
{T'}_{ac}^{B_4} &= -4k'_- \int_{z'_0}^{1} \frac{\partial u'}{\partial z'} \cosh(k'_+ (1-z'))dz' \\
{T'}_{ac}^{A_5} &= 4 \int_0^{1} \frac{\partial u'}{\partial z'} \frac{\partial^3 u'}{\partial {z'}^3} dz'
\end{aligned}
$$

The resonant frequencies, ω'_n, are those values which allow non-zero solutions to Equation (4.31). Thus, to determine the resonant frequencies of the CNT resonator, ω'_n which cause the 9x9 coefficient matrix in (4.31) to have zero determinant are found numerically. In particular, the lowest such ω'_n is found and assigned as ω'_0, the fundamental frequency of the CNT resonator. The effect of the nanomagnet on resonance frequency is determined by independently solving for two values of F_{mag}.

4.4 Results

The readout of the nanomagnet state will be performed by monitoring the resonant frequency of the CNT resonator. To benchmark the sensitivity of our technique, we calculate

the frequency shift that will be induced by a magnetic moment reversal of a single Bohr magneton magnitude ($\Delta m = 2\mu_B$). As an initial demonstration we consider a particular suspended CNT, called Device A, with: $L = 1\,\mu$m, $d = 1$ nm, the nanomagnet centered over the gate ($z_0 = \frac{L}{2}$), zero residual tension ($T_0 = 0$), and a gate-CNT separation of 200 nm, which gives a field gradient of $3 \cdot 10^5$ T/m. The shift in resonance frequency due to the $\Delta m = 2\mu_B$ transition is found to be maximum for a DC gate voltage of 59 mV in this device. The maximum frequency shift is $\Delta f_0 = 6.3$ kHz. For comparison, the CNT-torque sensing technique achieves a theoretical maximum 4 kHz frequency shift for $\Delta m = 24\mu_B$, using the same CNT device parameters and a CNT-nanomagnet grafting length of 0.5 nm [79]. We can further optimize the device sensitivity by examining how it depends on the device parameters.

4.4.1 Length and Diameter Dependence

The nanomagnet induced frequency shift will depend on many device parameters, including length and CNT diameter. Figure 4.3(a) and (b) show the calculated frequencies and frequency shifts, respectively, as a function of applied gate voltage for several resonator lengths, L. For each fixed L, there is a maximum frequency shift at a small, finite DC gate voltage, V_g^{max}. As L increases, V_g^{max} decreases while the magnitude of the frequency shift increases linearly with L (for parameter dependence fitting see appendix E). Comparing Figures 4.3(a) and (b), we see that a larger frequency shift corresponds to a lower resonance frequency. This can be understood as a longer CNT device having a lower spring constant, yielding both a lower resonance frequency and a larger displacement in response to an applied force.

In general, CNT resonators are very sensitive to the CNT diameter, as the bending rigidity is proportional to r^4. Figure 4.3(d) shows the frequency shift response for a 1 μm long CNT of three different diameters. Smaller CNTs produce much larger frequency shifts that occur at lower gate voltages. The maximum frequency shift (Δf_0 that occurs at V_g^{max}) is proportional to $r^{-7/2}$ (see appendix E for fitting). Figure 4.3(c) shows the resonance frequency for the same devices plotted in 4.3(d), where we see similar lower absolute frequencies for higher shifts as observed for length variation.

The gate voltage at which the maximum frequency shift occurs, V_g^{max}, can be understood by assessing the tension induced in the CNT by the gate voltage. Figures 4.3(e) and

4.3(f) show the frequency shifts for the same devices as in (b) and (d), respectively, now plotted as a function of the gate-induced tension scaled by the critical tension, $T_{crit} = \frac{EI}{L^2}$. At the critical tension, the restoring force from bending rigidity and tension, corresponding to the first two terms in the Euler-Bernoulli governing equation (4.13), are of equal magnitude. For the full range of CNT lengths and diameters considered here, the maximum frequency shift is found to occur at approximately $T \approx 6.3\,T_{crit}$. Hence, the maximum frequency shift occurs at a specific balance of restoring forces in the CNT, independent of the length and diameter. This optimal force balance can be reached for a wide range of devices by appropriate tuning of the DC gate voltage. Furthermore, this point can be approximately identified in the resonant frequency response of the CNT resonator, as a specific point along the transition between constant resonant frequency at low gate voltages and linear gate voltage dependence at high gate voltages, thus permitting pre-tuning of the magnetic force sensor.

4.4.2 Residual Tension

As briefly mentioned above, the fabrication and growth of suspended CNT devices can result in residual tension built into the CNT. Until now we have considered zero residual tension, however a range of residual tensions have been observed in the experimental literature, including [77, 39, 80] $T_0' \equiv T_0/T_{crit} = -26, -18, 0, 1$, and additional device engineering could permit other values. Figure 4.4(b) displays the frequency shift response for various residual tensions. Large residual compressions, $T_0' < -4\pi^2$, would result in buckling of the CNT [28] and are not considered here. However, residual compression within the buckling limit ($-4\pi^2 < T_0' < 0$) results in a significantly increased frequency shift compared to $T_0' = 0$. Fitting the maximum frequency shift (see appendix E) as a function of T_0', for various lengths and diameters, with T_0' ranging from -35 to 35, we find that the maximum frequency shift is approximately proportional to $(4\pi^2 + T_0')^{-1}$. Figure 4.4(a) shows the resonance frequency of the devices in 4.4(b). As before, a larger frequency shift is again seen with a lower resonance frequency. However, at voltages above V_g^{max}, the effects of residual tension are reduced and the three curves join at high voltages.

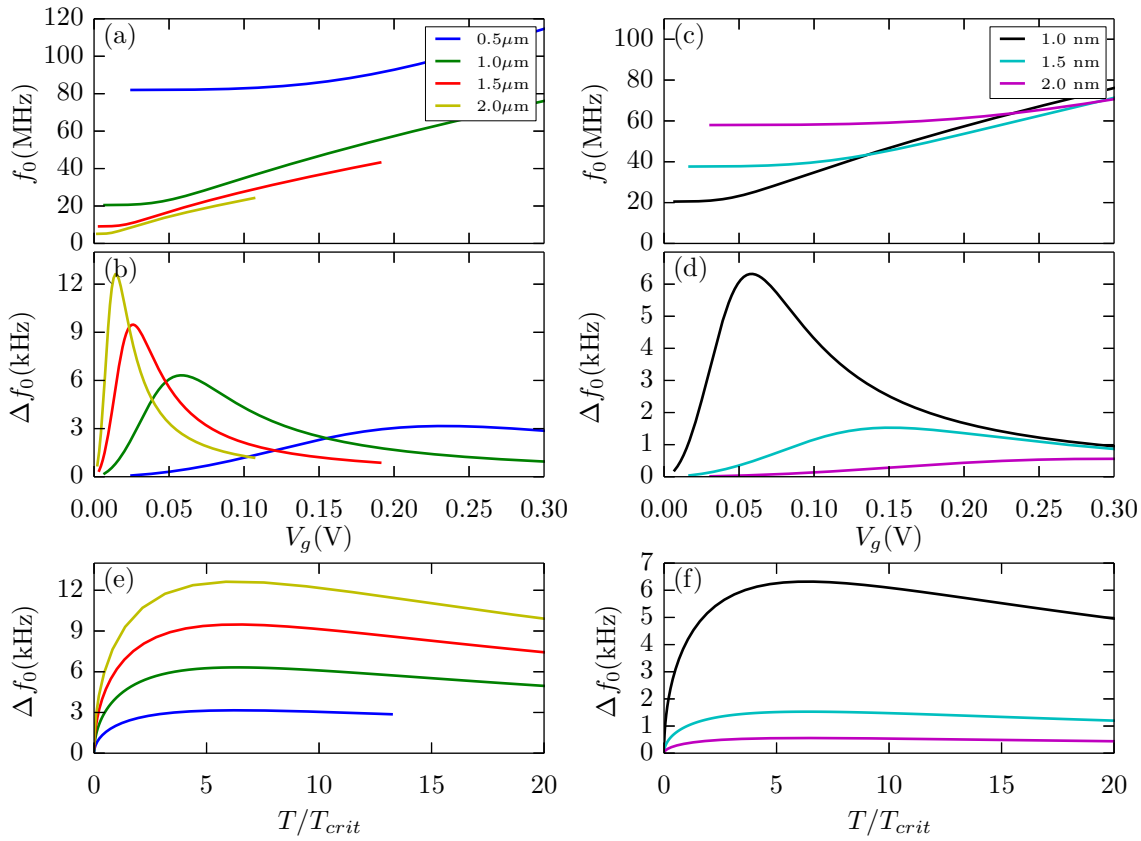

Figure 4.3: **a)** The resonance frequency versus gate voltage for various suspended CNT lengths, using $d = 1\,\text{nm}$, $h = 200\,\text{nm}$, $\frac{\partial B_z}{\partial x} = 3 \cdot 10^5\,\text{T/m}$. Note that all resonator behaviour is symmetric with respect to the sign of V_g. Numerical precision limits the range over which some curves are displayed. **b)** The gate voltage dependence of the resonance frequency shift produced by a nanomagnet magnetic transition of $\Delta m = 2\mu_B$, for the devices from (a). **c)** The resonant frequency of CNTs with various diameters, using $L = 1\,\mu\text{m}$, $h = 200\,\text{nm}$, $\frac{\partial B_z}{\partial x} = 3 \cdot 10^5\,\text{T/m}$. **d)** The frequency shift of the devices in (c). **e**,**f)** The frequency shifts from (b) and (d) respectively, versus tension scaled by the critical tension, T_{crit}.

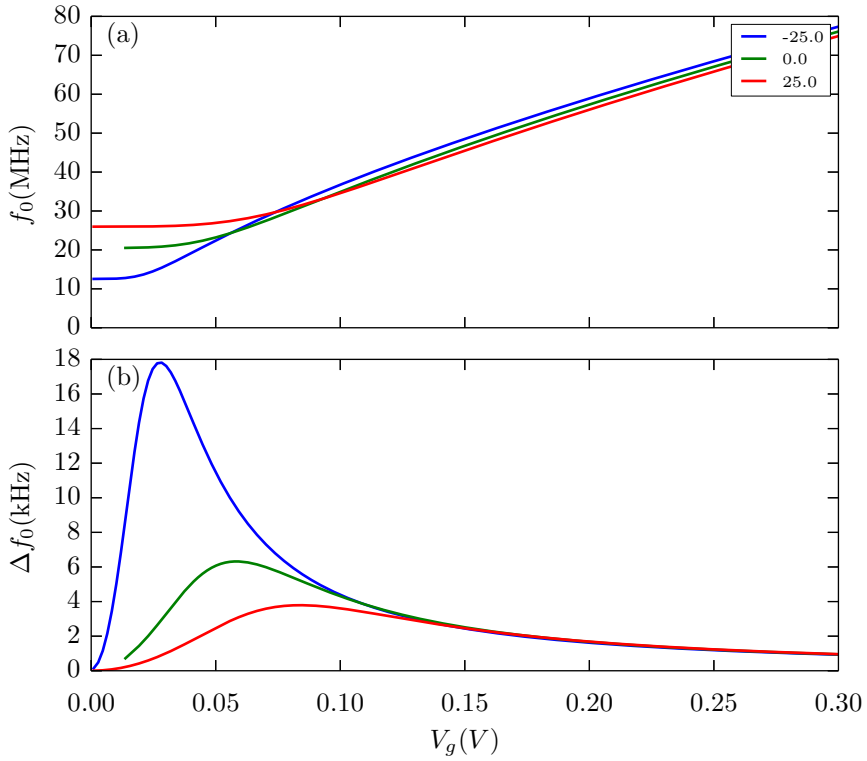

Figure 4.4: **a)** Resonant frequency and **b)** frequency shift using three values for residual CNT tension T_0/T_{crit}, and device parameters $L = 1\ \mu$m, $d = 1$ nm, $h = 200$ nm, $\frac{\partial B_z}{\partial x} = 3 \cdot 10^5$ T/m

4.4.3 Dependence on Lateral Nanomagnet Position

As a final device parameter to consider, we note that the position of the nanomagnet on the CNT will influence the sensitivity to changes in the magnetic moment. Firstly, the force on the nanomagnet will change as a result of the changing magnetic field gradient. Figure 4.5(a) shows the gradient of B_z as a function of the position along the CNT, for Device A and the gate geometry used for figure 4.2. In this device, the force will increase slightly as the nanomagnet is moved away from center, before decreasing rapidly near the ferromagnet edge. In addition to the change in force, the resonator response will depend on the position of the point force, via Equation 4.13. Figure 4.5(b) shows the maximum frequency shift for $\Delta m = 2\mu_B$, as a function of position for the same device parameters as 4.5a. A nanomagnet positioned anywhere in the central half of the CNT will have a maximum frequency shift of at least 50% of the optimal value attained for a centered nanomagnet ($z_0 = L/2$). This illustrates the robustness of this measurement technique to uncertainty in nanomagnet positioning.

4.5 Noise and readout bandwidth limits

To observe the frequency shifts calculated above, they will have to be observable in the presence of the noise in a real frequency measurement. As discussed in section 2.5, the ultimate limits on resonator noise will be determined by thermomechanical noise of the CNT resonator, with the minimum detectable frequency shifts given by equation (2.25) in the slow measurement regime ($\tau \gg \frac{Q}{2\pi f_0}$) and equation (2.26) in the fast measurement regime ($\tau \to 0$).

Using the high Q factors measured in previous experiments[39], $Q = 10^5$, along with a device temperature of 100 mK, and $\langle v_{max}^2 \rangle = (0.25\,\text{nm})^2$, the minimum detectable frequency shift signal of Device A at the optimal gate voltage ($V_g^{dc} = 59$ mV), with a 1 Hz measurement bandwidth is 5.4 Hz. In the infinite bandwidth limit, given by Equation (2.26), the minimum detectable frequency shift for the same device and gate setting is 270 Hz. Thus, the $\Delta m = 2\mu_B$ transition, which results in $\Delta f_0 = 6.3$ kHz, exceeds the intrinsic thermomechanical resonator noise for arbitrarily short measurement times in this device.

Another readout limiting factor for the CNT resonator will be given by the mechanical

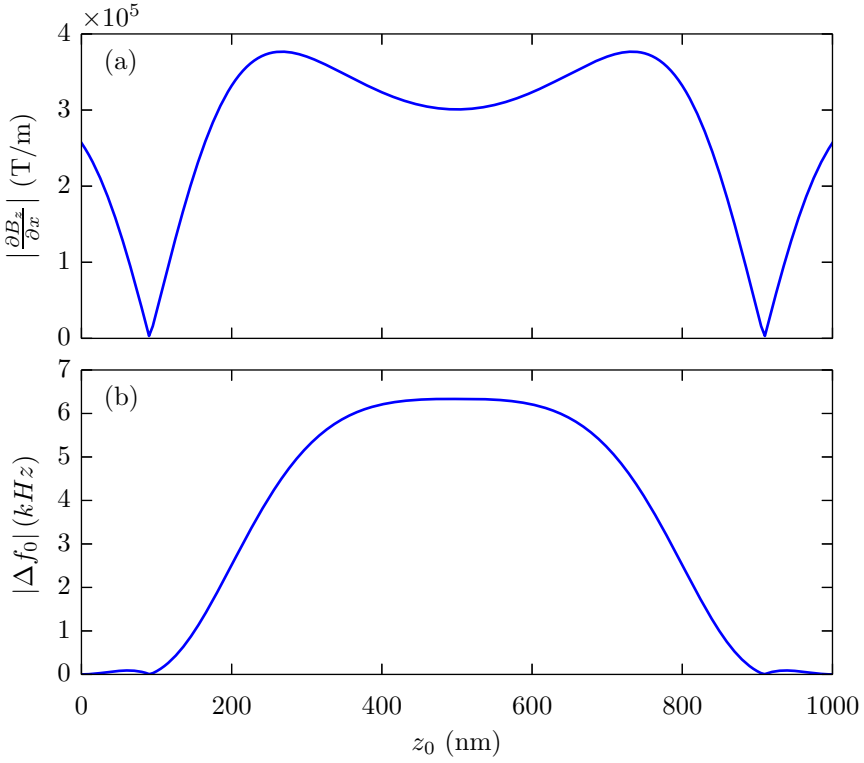

Figure 4.5: **a)** The absolute magnetic field gradient $\frac{\partial B_z}{\partial x}$ as a function of position along the CNT, for the 800 nm wide by 200 nm thick cobalt gate and 200 nm gate-CNT separation. **b)** The maximum frequency shift of Device A for $\Delta m = 2\mu_B$, as a function of nanomagnet position.

response of the CNT to a resonant frequency shift. The observable mechanical state of the CNT will have a transient response following the frequency shift. This transient response is characterized by a ring down timescale, $\tau_m \sim \frac{Q}{4\pi f_0}$. For Device A, and $Q = 10^5$, the ring down timescale is $\tau_m \sim 300\,\mu$s. The electrical measurement bandwidth for CNT resonators should exceed this timescale through the use of fast readout [42] and cryogenic amplifiers, which typically operate at MHz to GHz bandwidths. Thus, we expect the mechanical ring down time to be the bandwidth limiting timescale in these devices.

Table 4.1 displays the ring down times and calculated signal to noise ratios for fast readout of five example devices, where signal to noise is defined as

$$\mathrm{SNR}_\infty = \max_{V_g} \frac{\Delta f_0}{\delta f_0|_{\tau=0}} \tag{4.32}$$

and $\delta f_0|_{\tau=0}$ is evaluated using $\langle v_{max}^2 \rangle = \left(\frac{Q V_g^{dc} V_g^{ac} C_g'}{4\pi^2 m' f_0^2}\right)^2$, $m' \approx m/2$ which is evaluated from the calculated mode shapes, and $V_g^{ac} = 5\ \mu$V, which is chosen to keep these devices in the linear regime. The Devices B-E each have one parameter altered with respect to Device A. For each device, two quality factor models are considered. In one case, a fixed value of $Q = Q^*$ is used, where $Q^* = 10^5$ for Devices A-D. The other case uses a fixed damping factor $\eta = \frac{2\pi f_0}{Q^*}$. In both cases, increasing length and residual compression, and decreasing diameter, improve signal to noise ratio. In the case of constant quality factor, the increased signal to noise comes at the cost of increased mechanical ring down time. Decreasing quality factor, as in Device E, decreases $\mathrm{SNR}_\infty \propto Q^{-1}$ while linearly decreasing ring down time. The signal to noise ratio and ring down times may be adjusted through device design to obtain sufficient signal at a desired time scale.

It should be noted that the above results are for linear resonator sensing. If additional sensitivity is required, non-linear resonator behaviour can be used to measure the resonance frequency shifts, as was done in reference [6]. Alternatively, as discussed in section 2.4.4, the ultrasensitive measurement technique can be used to observe the frequency of parameter modulation. This could be used in conjunction with external driving of the nanomagnetic state (eg, via Rabi oscillations of single molecule magnet spin states) to measure the state oscillation frequency and the related coupling strengths.

Device	Change	$\mathbf{SNR}^1_\infty$	$\mathbf{SNR}^2_\infty$	τ^1_m (μs)	τ^2_m (μs)
A	None	62	31	320	160
B	$L = 2\mu$m	700	86	1300	160
C	$d = 1.5$nm	11	10	170	160
D	$T_0' = -25$	220	67	520	160
E	$Q^* = 3000$	1.9	0.9	9.6	4.8

Table 4.1: Infinite bandwidth signal to noise ratios for $\Delta m = 2\mu_B$, and ring down times, for example CNT devices. Device A has $L = 1\ \mu\text{m}, d = 1\ \text{nm}, T_0' = 0, Q^* = 10^5$. Devices B-E have one parameter changed with respect to Device A. SNR^1_∞ and τ^1_m use $Q = Q^*$. SNR^2_∞ and τ^2_m use $\frac{f_0}{Q} = \frac{50\ \text{MHz}}{Q^*}$.

4.6 Discussion

One of the motivating applications of this CNT magnetic force detection scheme is towards the study of single molecule magnets (SMMs). The CNT-torque technique was used to observe magnetic reversal in the S=6 $TbPc_2$ SMMs [6]. Our measurement scheme would permit similar measurements, over a wide range of SMMs. Beyond magnetic reversal measurements, the improved sensitivity of our technique should enable single shot readout of SMM magnetic states. The g-factors of SMM spins are approximately $g \approx 2$, meaning that $\Delta S = 1$ transitions are approximately equivalent to the $\Delta m = 2\mu_B$ transitions we consider above. This could allow us to probe every state transition in the SMM spin, including coherent spin dynamics that have been demonstrated in a number of SMMs including V_{15} [81], Cr_7Mn and Cr_7Ni [82], and Fe_8 [83, 84, 85]. Driving of the coherent transitions with an external microwave field is compatible with our sensing, as long as the driving frequencies are well separated from the CNT mechanical frequencies, allowing these coherent transitions to be externally driven while being measured by our technique. This would allow the coherent SMM spin rotations to be observed within the parameters described in table 4.1.

As a particular example, at 1.2 K the Cr_7Ni and Cr_7Mn SMMs have spin relaxation times (T_1) on the order of 1 ms in bulk crystals [82]. If this relaxation timescale is maintained or exceeded for individual SMMs grafted to CNTs, the devices considered here could enable single shot spin state measurements. This readout could be used to evaluate spin decoherence and relaxation timescales of individual SMMs. These experiments

could provide further exploration of relaxation mechanisms in the SMMs by observing the dependence of the relaxation time on the applied magnetic field, and on the mechanical resonator properties such as a 1D phonon density. Even beyond these applications, the ring down time scale of Device E presented in table 4.1 is comparable to the 4 μs spin decoherence time achieved with deuterated Cr_7Ni [82], potentially permitting readout on the timescale of decoherence.

Chapter 5

Summary and Conclusion

CNT resonators have been developed into some of the most sensitive measurement devices to date. In this thesis, we describe work towards applying CNT resonators to sensing of the magnetic states of nanoscale magnetic objects, such as single molecule magnets. We have developed fabrication of CNT resonators using a local fine gate, to both enable the strong magnetic field gradient that will be used to couple the nanomagnet to the resonator and to minimize crosstalk capacitances to the source and drain. We have developed a CVD process capable of growing low-defect CNTs across the raised source and drain contacts. Analysis of as-grown devices have identified some remaining device complications. Proposed methods of correcting these issues have been discussed.

In addition to the nanofabrication of devices, numerical simulation of the proposed sensing technique has been completed. Modelling of the CNT resonator and the magnetic field gradient induced force on the nanomagnet enable extraction of the resonant frequency and its dependence on nanomagnet state. By exploring the impact of device operating and fabrication parameters, we have identified preferred device properties and optimal operating conditions for maximum sensitivity. Our proposed technique presents at least an order of magnitude improvement over the most recent magnetic moment sensing techniques. This sensitivity should allow measurement of single electron spin flips at sub-millisecond timescale, with the potential for ~ 10 μs measurement times if ideal noise measurements can be employed. This proposed sensing technique will enable novel studies of magnetic systems at the nanoscale, such as single shot readout of single molecule magnet states.

APPENDICES

Appendix A

Suspended CNT Device Fabrication Process

This appendix describes the details of the most recent suspended CNT device fabrication process, using the QNCFab facilities for all but the CVD process. The standard lithography recipes are described following the device recipe.

The devices are fabricated on a 4" Si wafer with 300 nm SiO_2 thermal resist. The wafer is intrinsic Si with resistivity $\rho > 5000\ \Omega/\text{cm}$, and $\langle 100 \rangle$ orientation.

1. Clean wafer as required by wafer condition
2. Source/Drain definition:
   (a) Photolithography using PMGI-S1805 Bilayer Recipe and CNT Mask #1 (SD)
   (b) Deposit 10nm Ti, followed by 40nm Pt, using the Ti/Pt recipe in the IntlVac e-Beam evaporation system
   (c) Liftoff in PG remover
   (d) 2 minute descum in YES-CV200RFS PR Stripper
3. Trench Etching:
   (a) Photolithography using S1811 Monolayer Recipe and CNT Mask #2 (Trench)

(b) Partially etch SiO_2 using Oxford III-V etcher. Use OPT-SiO2 for 40s to etch $\sim$ 240 nm

(c) Liftoff in acetone

(d) Main ash recipe (1000W RF, 180 °C) in YES-CV200RFS PR Stripper to remove any remaining S1811

4. Gate Pad Definition:

(a) Photolithography using PMGI-S1805 Bilayer Recipe and CNT Mask #3 (Gate)

(b) Deposit 10nm Ti, followed by 40nm Pt, using the Ti/Pt recipe in the IntlVac e-Beam evaporation system

(c) Liftoff in PG remover

(d) 2 minute descum in YES-CV200RFS PR Stripper

5. Fine gate definition:

(a) Electron beam lithography using the PMMA-PMMA bilayer recipe and CNTFineGate pattern

(b) Deposit 10nm Ti, followed by 40nm Pt, using the Ti/Pt recipe in the IntlVac e-Beam

(c) Liftoff in PG remover

6. CNT Catalyst Deposition:

(a) Photolithography using PMGI-S1805 bilayer recipe and CNT Mask #4 (Islands)

(b) 4 minutes of 50W descum in YES-CV200RFS PR Stripper

(c) Spin on 8X Catalyst Solution (see appendix B) using the following spin settings:

i. 100 RPM at 100 RPM/s for 25s

ii. 2000 RPM at 500 RPM/s for 45s

iii. 0 RPM at 500 RPM/s for 0s

(d) Bake sample at 120 °C for 5 minutes.

(e) Liftoff in PG remover. Use 30s PG remover soak, followed by separate 15 minute PG remove soak to minimize catalyst re-adhesion.

(f) 6 minutes of 50W descum in YES-CV200RFS PR Stripper, to remove any final resist residues.

7. CVD growth of CNTs using methane recipe #2 (see Appendix B)

A.1 PMGI-S1805 Bilayer Photolithography Recipe

The basic recipe for our bilayer photolithography is:

1. Clean sample as required
2. Apply a hexamethyl disilazane (HMDS) coat using the YES-310-TA HMDS Oven recipe #1.
3. Spin PMGI onto sample using the Wafer spinner, with the following spin settings
   (a) 500 RPM at 100 RPM/s ramp for 5s
   (b) 5000 RPM at 500 RPM/s ramp for 60s
   (c) 0 RPM at 500 RPM/s ramp for 0s
4. Bake sample at 150 °C for 5 minutes. If slightly less undercut is desired after development, this temperature can be increased to 190 °C.
5. Spin Shipley S1805 photoresist onto the sample, using the same spinning recipe as the PMGI layer.
6. Bake sample at 120 °C for 90s
7. Expose sample using MA6 Mask Aligner and desired photomask. The nominal exposure time is 4.0s, however the best resolution exposure settings will depend on feature size, substrate, and lamp lifecycle.
8. Develop sample for 60s in MF-319 developer, followed by 60s DI water to stop development. Rinse in DI water and blow dry with N_2.
9. Clean sample with 2 minute, 50W descum recipe in YES-CV200RFS PR Stripper to remove the HMDS layer in the developed regions.

The nominal resist thicknesses are $\sim$ 500 nm PMGI and $\sim$ 500 nm S1805. The minimum reliable line separation distance was found to be ≈ 2 μm, as narrower line separations would often result in the PMGI layer being completely removed resulting in layer collapse and subsequent liftoff issues.

A.2 S1811 Monolayer Photolithography Recipe

The basic recipe for our monolayer photolithography is:

1. Clean sample as required
2. Spin Shipley S1811 photoresist onto the sample, using the same spinning recipe as the PMGI layer in A.1
3. Bake sample at 120 °C for 90s
4. Expose sample using MA6 Mask Aligner and desired photomask. The nominal exposure time is 4.0s, however the best resolution exposure settings will depend on feature size, substrate, and lamp lifecycle.
5. Develop sample for 60s in MF-319 developer, followed by 60s DI water to stop development. Rinse in DI water and blow dry with N_2.

The nominal resist thickness is 1 μm.

A.3 PMMA-PMMA Bilayer Electron Beam Lithography Recipe

The basic recipe for our bilayer EBL is:

1. Clean sample as required
2. Spin PMMA 495k A3 resist onto sample using the Wafer spinner, with the following spin settings

   (a) 500 RPM at 500 RPM/s ramp for 10s
   (b) 2000 RPM at 2000 RPM/s ramp for 40s
   (c) 0 RPM at 500 RPM/s ramp for 0s

3. Bake sample at 180 °C for 3 minutes.

4. Spin PMMA 950k A4 resist onto the sample, using:
   (a) 500 RPM at 500 RPM/s ramp for 10s
   (b) 2800 RPM at 2000 RPM/s ramp for 40s
   (c) 0 RPM at 500 RPM/s ramp for 0s

5. Bake sample at 180 °C for 12 minutes.

6. Expose sample using RAITH 150TWO electron-beam direct-write lithography system. Exposure settings will depend on sample. The nominal settings used in this work are 20 kV accelerating voltage, 30 μm aperture, 280 C/μm^2 area dose.

7. Develop sample for 45s in IPA:DI (7:3), followed by 45s in DI water.

Appendix B

CNT CVD Recipes

This appendix details the primary CVD recipes tested for CNT growth. All growths were performed in sealed quartz tube CVDs. The ethanol CVD was performed in a 2" quartz tube. The ethylene and methane CVD were performed in a 1" quartz tube.

B.1 Catalyst Recipe

All CVD growths used a Fe-Co-Mo catalyst with silica supporting crystals. The support liquid and concentrations were adjusted to affect catalyst distribution and density. The final recipe for the catalyst solution, referred to as "8X Catalyst Solution", is:

1. In a small glass vial, combine:
   (a) 1.4 mg of Molybdenum (II) acetate dimer ($Mo_2(OCOCH_3)_4$)
   (b) 9.2 mg of Cobalt (II) acetate ($(CH_3CO_2)_2Co$)
   (c) 6.0 mg of Iron (III) acetylacetonate ($Fe(C_5H_7O_2)_3$)
   (d) 3.0 mL of IPA
2. In a separate glass vial, combine:
   (a) 15.0 mg of fumed Silica 7nm nanobeads

(b) 3.0 mL of IPA

3. Sonicate both vials for $\sim$ 1 hour
4. Combine 2mL of each solution into a separate glass vial
5. Sonicate the combined solution for $\sim$ 2 hours

B.2 Ethanol CVD

1. Ramp to 850 °C under 1200 sccm Ar and 36 sccm H_2 (30 minutes)
2. At 850 °C, flow 36 sccm H_2 through ethanol bubbler then to CVD, and flow 1200 sccm Ar normally
3. Cool to 80 °C under 1200 sccm Ar and 36 sccm H_2 (60 minutes)

B.3 Ethylene CVD

1. Ramp to 850 °C, under 300 sccm Ar and 10 sccm H_2 (20 minutes)
2. At 850 °C, flow 300 sccm Ar, 10 sccm H_2 and 20 sccm C_2H_4 (20 minutes)
3. Cool to 80 °C under 300 sccm Ar and 10 sccm H_2 (40 minutes)

B.4 Methane CVD

B.4.1 Recipe #1

1. Ramp to 850 °C under 40 sccm H_2 (20 minutes)
2. At 850 °C, flow 200 sccm CH_4 and 40 sccm H_2 (20 minutes)
3. Cool to 80 °C under 40 sccm H_2 (40 minutes)

B.4.2 Recipe #2

1. Ramp to 850 °C under 440 sccm H_2 and 600 sccm Ar (20 minutes)
2. At 850 °C, flow 1000 sccm CH_4 and 440 sccm H_2 (20 minutes)
3. Cool to 80 °C under 440 sccm H_2 and 600 sccm Ar (40 minutes)

B.5 CVD Cleaning and Conditioning

Each CVD growth was preceded by a cleaning and conditioning process to ensure the tube contamination was minimized. The process was similar for each growth. The exact process used for the final methane CVD growths is included here:

1. Open quartz tube to ambient air
2. Ramp to 850 °C (20 minutes)
3. Wait 30minutes
4. Cool to 80 °C ($\sim$40 minutes)
5. Reseal quartz tube
6. Ramp to 850 °C under 200 sccm H_2 flow (20 minutes)
7. At 850 °C, flow 1000 sccm CH_4 and 200 sccm H_2 (30 minutes)
8. Cool to 80 °C under 200 sccm H_2 flow ($\sim$ 40 minutes)

Appendix C

Zero Bias Conductance Peak Fitting

The Coulomb peaks broadening can be dominated by either tunneling or thermal effects. Figure C.1 shows the results of fitting three of the experimentally measured zero bias conductance peaks from figure 3.12. The tunneling limited conductance is fitted using[60]

$$\frac{G_{tunnel}}{G_{max}} = \frac{(\Gamma/2\alpha)^2}{(V_g - V_{g,0})^2 + (\Gamma/2\alpha)^2} \tag{C.1}$$

where Γ is the tunnel coupling of the CNT, G_{max} is the maximum conductance of the conductance peak, $V_{g,0}$ is the central gate voltage of the peak, and

$$\alpha = \frac{1}{1.32}\frac{C_g}{C_s + C_d + C_g} \tag{C.2}$$

The thermally limited conductance is fitted using [25]

$$\frac{G_{thermal}}{G_{max}} = \frac{\delta/k_BT}{2\sinh(\delta/k_BT)} \approx \frac{1}{2}\cosh^{-2}\left(\frac{\delta}{2.5k_BT}\right) \tag{C.3}$$

where

$$\delta = e\frac{C_g}{C_s + C_d + C_g}\,|V_g - V_{g,0}| \tag{C.4}$$

As expected from the calculated tunneling rates in section 3.4 ($\Gamma \sim 2$ GHz $= 15mK$), the thermal limited fitting provides a much better fit for the Coulomb valleys. The thermal fitting achieves the best fit using $T = 1.6$ K and Coulomb peak heights $G_{peak} \approx 0.016$ e$^2/h$, indicating that our sample was at a higher temperature than expected.

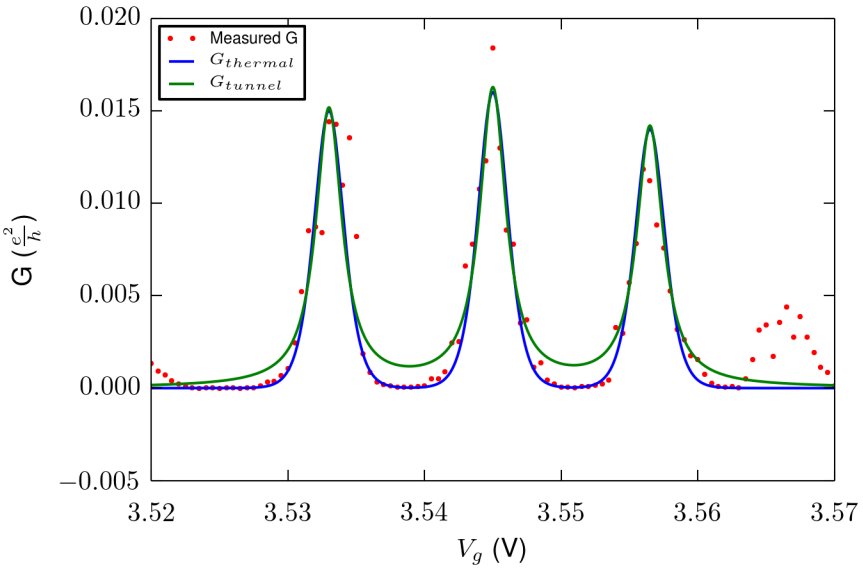

Figure C.1: The measured zero bias conductance peaks for the suspended CNT device, and fitting of these curves using tunneling and thermally limited conductance models.

Appendix D

Magnetic field of ferromagnetic gate

This calculation is based on [86]. The magnetic field of the rectangular ferromagnetic gate can be described by the scalar field Φ, where outside of the magnet the field relation is

$$\vec{B}(\vec{r}) = -\mu_0 \nabla \Phi(\vec{r}) \tag{D.1}$$

The scalar field is calculated as

$$\phi(\vec{r}) = -\frac{1}{4\pi} \nabla \int_V \frac{\vec{M}(\vec{r'})}{\left|\vec{r} - \vec{r'}\right|} d\vec{r'} \tag{D.2}$$

where $\vec{M}(\vec{r'})$ is the magnetization and V is the three-dimensional ferromagnet.

In our system of interest, M is constant along the z axis, so $\vec{M}(\vec{r}) = M_0 \hat{e}_z$. The integral then becomes

$$\phi(\vec{r}) = -\frac{M_0}{4\pi} \frac{\partial}{\partial z} \int_{-z_c}^{z_c} \int_{-y_c}^{y_c} \int_{-x_c}^{x_c} \left[\frac{1}{\sqrt{(x-x')^2 + (y-y')^2 + (z-z')^2}} \right] dx' dy' dz' \tag{D.3}$$

where $2x_c$ is the gate thickness, $2y_c$ is the gate length, and $2z_c$ is the gate width.

The solution to (D.3) is given in [86]:

$$B_x = \frac{\mu_0 M_0}{4\pi} \sum_{k,l,m=1}^{2} (-1)^{k+l+m} \ln \left(y + (-1)^l y_c + \sqrt{(x + (-1)^k x_c)^2 + (y + (-1)^l y_c)^2 + (z + (-1)^m z_c)^2)} \right) \tag{D.4}$$

$$B_y = \frac{\mu_0 M_0}{4\pi} \sum_{k,l,m=1}^{2} (-1)^{k+l+m} \ln\left(x + (-1)^k x_c + \sqrt{(x + (-1)^k x_c)^2 + (y + (-1)^l y_c)^2 + (z + (-1)^m z_c)^2)}\right) \tag{D.5}$$

$$B_z = \frac{\mu_0 M_0}{4\pi} \sum_{k,l,m=1}^{2} (-1)^{k+l+m} \frac{(y + (-1)^l y_c)(z + (-1)^m z_c)}{|y + (-1)^l y_c|\,|z + (-1)^m z_c|} \cdot \operatorname{atan}\left(\frac{\left|y + (-1)^l y_c\right| \left(x + (-1)^k x_c\right)}{|z + (-1)^m z_c| \sqrt{(x + (-1)^k x_c)^2 + (y + (-1)^l y_c)^2 + (z + (-1)^m z_c)^2)}}\right) \tag{D.6}$$

Appendix E

Parameter dependence of the maximum frequency shift

To extract the relationship between device parameters and the maximum frequency shift, we determined the maximum shift for a range of device values and used numerical fitting to determine the corresponding relation. The calculations below used initial parameters of $L = 1\ \mu$m, $r = 0.5$ nm, $z_0 = \frac{L}{2}$,$T_0 = 0$, $h = 200$ nm, and a magnetic field gradient of $3 \cdot 10^5$ T/m. All of the fittings shown below have $R^2 = 1.000$ with respect to the displayed data points.

The length dependence is shown in Figure E.1, using L from 600 nm to 2 μm. The calculated fitting is

$$\max(\Delta f) \propto L^{1.000} \tag{E.1}$$

The diameter dependence is examined with d ranging from 1 nm to 2.5 nm. The maximum frequency shift relationship is shown in Figure E.2. The calculated fitting is

$$\max(\Delta f) \propto d^{-3.500} \tag{E.2}$$

The maximum shift for residual tension ranging from $-35L^2/(EI)$ to $35L^2/(EI)$ is shown in Figure E.3. The calculated fitting is

$$\max(\Delta f) \propto \left(T_0' + 4\pi^2\right)^{-1.027} \tag{E.3}$$

where $T_0' = T_0 L^2/(EI)$.

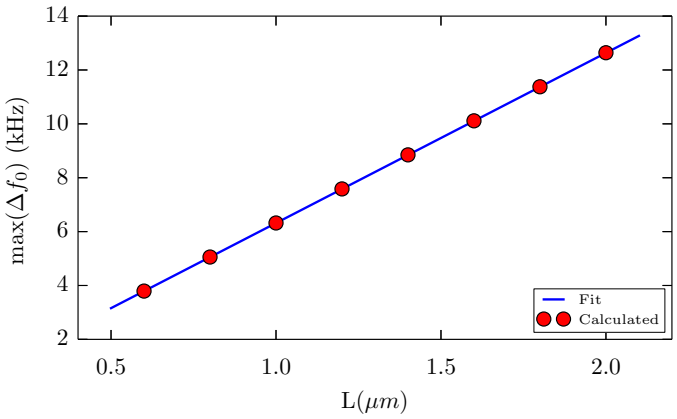

Figure E.1: Calculated maximum frequency shift as a function of resonator length, L, and the calculated fit.

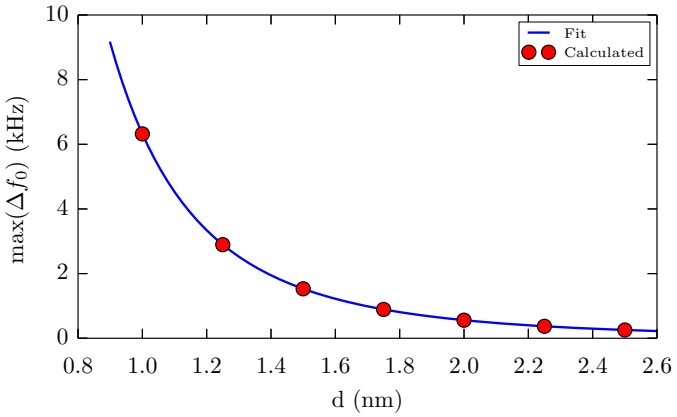

Figure E.2: Calculated maximum frequency shift as a function of CNT diameter, d, and the calculated fit.

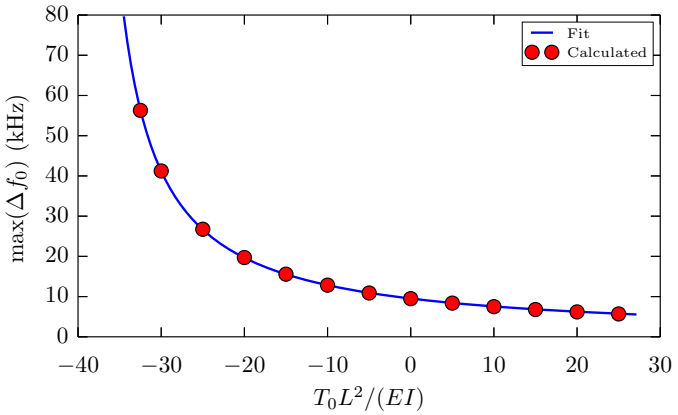

Figure E.3: Calculated maximum frequency shift as a function of residual tension, T_0, and the calculated fit.

Appendix F

Errata to J. Appl. Phys. 115 114501

The following corrections apply to

> Willick K, Haapamaki C, Baugh J. Sensitive magnetic force detection with a carbon nanotube resonator. J Appl Phys. **115** 114501 (2014)

The coefficients of δf_0 formula are incorrect. Equation (9) should read

$$\delta f_0 = \frac{1}{2\pi}\sqrt{\frac{k_B T}{2\pi m' \left\langle v_{max}^2 \right\rangle \tau f_0 Q}} \tag{F.1}$$

and equation (10) should be

$$\delta f_0|_{\tau \approx 0} = \frac{1}{2\pi}\sqrt{\frac{\pi k_B T}{2m' \left\langle v_{max}^2 \right\rangle Q^2}} \tag{F.2}$$

In the paragraph following equation (10), the driving amplitude should be changed from $\langle v_{max}^2 \rangle = (0.1 \text{ nm})^2$ to $\langle v_{max}^2 \rangle = (0.25 \text{ nm})^2$. The infinite bandwidth limit minimum detectable frequency shift should be 270 Hz instead of 86 Hz.

In the line immediately following equation (11), it should read:

and $\delta f_0|_{\tau=0}$ is evaluated using $\langle v_{max}^2 \rangle = \left(\frac{Q V_g^{dc} V_g^{ac} C_g'}{4\pi^2 m' f_0^2}\right)^2$, and $V_g^{ac} = 5\,\mu\text{V}$.

References

[1] W. Wernsdorfer. Molecular nanomagnets: towards molecular spintronics. *Int. J. Nanotechnol.*, 7(4/5/6/7/8):497–522, 2010.

[2] H. van Houten and C. Beenakker. Quantum point contacts. *Physics Today*, 49(7):22–27, 1996.

[3] S. Komiyama, O. Astafiev, V. Antonov, T. Kutsuwa, and H. Hirai. A single-photon detector in the far-infrared range. *Nature*, 403:405, 2000.

[4] D. Rugar, R. Budakian, H. J. Mamin, and B. W. Chui. Single spin detection by magnetic resonance force microscopy. *Nature*, 430(6997):329–332, July 2004.

[5] D. Vasyukov, Y. Anahory, L. Embon, D. Halbertal, J. Cuppens, L. Neeman, A. Finkler, Y. Segev, Y. Myasoedov, M. L. Rappaport, M. E. Huber, and E. Zeldov. A scanning superconducting quantum interference device with single electron spin sensitivity. *Nat. Nanotechnol.*, 8(9):639–44, September 2013.

[6] M. Ganzhorn, S. Klyatskaya, M. Ruben, and W. Wernsdorfer. Carbon nanotube nanoelectromechanical systems as magnetometers for single-molecule magnets. *ACS nano*, 7(7):6225–36, July 2013.

[7] K. Jensen, K. Kim, and A. Zettl. An atomic-resolution nanomechanical mass sensor. *Nat. Nanotechnol.*, 3(9):533–537, 2008.

[8] B. Lassagne, D. Garcia-Sanchez, A. Aguasca, and A. Bachtold. Ultrasensitive mass sensing with a nanotube electromechanical resonator. *Nano Lett.*, 8(11):3735–3738, 2008.

[9] H.-Y. Chiu, P. Hung, H. W. C. Postma, and M. Bockrath. Atomic-scale mass sensing using carbon nanotube resonators. *Nano Lett.*, 8(12):4342–6, December 2008.

[10] J. Chaste, A. Eichler, J. Moser, G. Ceballos, R. Rurali, and a. Bachtold. A nanomechanical mass sensor with yoctogram resolution. *Nat. Nanotechnol.*, 7(5):301–4, May 2012.

[11] J. Moser, J. Güttinger, A. Eichler, M. J. Esplandiu, D. E. Liu, M. I. Dykman, and A. Bachtold. Ultrasensitive force detection with a nanotube mechanical resonator. *Nat. Nanotechnol.*, 8(7):493–496, July 2013.

[12] H.-S. P. Wong and D. Akinwande. *Carbon Nanotube and Graphene Device Physics*. Cambridge University Press, 2011.

[13] W. Izumida, K. Sato, and R. Saito. SpinOrbit Interaction in Single Wall Carbon Nanotubes: Symmetry Adapted Tight-Binding Calculation and Effective Model Analysis. *J. Phys. Soc. Japan*, 78(7):074707, July 2009.

[14] E. A. Laird, F. Kuemmeth, G. Steele, K. Grove-Rasmussen, J. Nygård, K. Flensberg, and L. P. Kouwenhoven. Quantum transport in carbon nanotubes. 2014.

[15] M. Huang, Y. Wu, B. Chandra, H. Yan, Y. Shan, T. Heinz, and J. Hone. Direct Measurement of Strain-Induced Changes in the Band Structure of Carbon Nanotubes. *Phys. Rev. Lett.*, 100(13):136803, April 2008.

[16] J. Svensson and E. E. B. Campbell. Schottky barriers in carbon nanotube-metal contacts. *J. Appl. Phys.*, 110(11):111101, 2011.

[17] Y.-C. Tseng and J. Bokor. Characterization of the junction capacitance of metal-semiconductor carbon nanotube Schottky contacts. *Appl. Phys. Lett.*, 96(1):013103, 2010.

[18] A. Javey, J. Guo, Q. Wang, M. Lundstrom, and H. Dai. Ballistic carbon nanotube field-effect transistors. *Nature*, 424(6949):654–7, August 2003.

[19] L. Ding, S. Wang, Z. Zhang, Q. Zeng, Z. Wang, T. Pei, L. Yang, X. Liang, J. Shen, Q. Chen, R. Cui, Y. Li, and L.-m. Peng. Y-Contacted High Performance n-Type Single-Walled Carbon Nanotube Field-Effect Transistors : Scaling and Comparison with Sc-Contacted Devices. *Nano Lett.*, 9(12):4209–4214, 2009.

[20] M. J. Biercuk, S. Ilani, C. M. Marcus, and P. L. Mceuen. Electrical Transport in Single-Wall Carbon Nanotubes. In *Carbon Nanotub. Adv. Top. Synth. Struct. Prop. Appl.*, volume 493, pages 455–493. Springer Berlin Heidelberg, 2008.

[21] F. Léonard and A. Talin. Size-Dependent Effects on Electrical Contacts to Nanotubes and Nanowires. *Phys. Rev. Lett.*, 97(2):026804, July 2006.

[22] W. Kim, A. Javey, R. Tu, J. Cao, Q. Wang, and H. Dai. Electrical contacts to carbon nanotubes down to 1nm in diameter. *Appl. Phys. Lett.*, 87(17):173101, 2005.

[23] Y. Zhang, N. W. Franklin, R. J. Chen, and H. Dai. Metal coating on suspended carbon nanotubes and its implication to metal tube interaction. *Chem. Phys. Lett.*, 331(November):35–41, 2000.

[24] D. Mann, A. Javey, J. Kong, Q. Wang, and H. Dai. Ballistic Transport in Metallic Nanotubes with Reliable Pd Ohmic Contacts. *Nano Lett.*, 3(11):1541–1544, November 2003.

[25] L. P. Kouwenhoven, C. M. Marcus, P. L. Mceuen, S. Tarucha, and M. Robert. Electron transport in quantum dots. In *Proc. NATO Adv. Study Inst. Mesoscopic Electron Transp.*, pages 105–214. Kluwer Series E345, 1997.

[26] R. Hanson, J. R. Petta, S. Tarucha, and L. M. K. Vandersypen. Spins in few-electron quantum dots. *Rev. Mod. Phys.*, 79(4):1217–1265, October 2007.

[27] S. Sapmaz, P. Jarillo-Herrero, L. P. Kouwenhoven, and H. S. J. V. D. Zant. Quantum dots in carbon nanotubes. *Semicond. Sci. Technol.*, 21(11):S52–S63, November 2006.

[28] M. Poot. *Mechanical systems at the nanoscale*. Phd, Technische Universiteit Delft, 2009.

[29] J.-P. Salvetat, J.-M. Bonard, N. H. Thomson, A. J. Kulik, L. Forro, W. Benoit, and L. Zuppiroli. Mechanical Properties of Carbon Nanotubes. *Appl. Phys. A Mater. Sci. Process.*, 69:255–260, 1999.

[30] A. Krishnan, E. Dujardin, T. Ebbesen, P. Yianilos, and M. Treacy. Youngs modulus of single-walled nanotubes. *Phys. Rev. B*, 58(20):14013–14019, November 1998.

[31] J. O. Island, V. Tayari, A. C. McRae, and A. R. Champagne. Few-Hundred GHz Carbon Nanotube Nanoelectromechanical Systems (NEMS). *Nano Lett.*, 12(9):4564–4569, September 2012.

[32] H. B. Meerwaldt. *Carbon nanotubes as electromechanical resonators: Single-electron tunneling, non-linearity, and high-bandwidth readout*. Phd, TU Delft, 2013.

[33] A. K. Hüttel, M. Poot, B. Witkamp, and H. S. J. van der Zant. Nanoelectromechanics of suspended carbon nanotubes. *New J. Phys.*, 10(9):095003, September 2008.

[34] S. Sapmaz, Y. Blanter, L. Gurevich, and H. van der Zant. Carbon nanotubes as nanoelectromechanical systems. *Phys. Rev. B*, 67(23):235414–, June 2003.

[35] V. Sazonova, Y. Yaish, H. Ustünel, D. Roundy, T. a. Arias, and P. L. McEuen. A tunable carbon nanotube electromechanical oscillator. *Nature*, 431(7006):284–7, September 2004.

[36] V. Sazonova. *A tunable carbon nanotube resonator*. Phd, Cornell University, 2006.

[37] V. Gouttenoire, T. Barois, S. Perisanu, J.-L. Leclercq, S. T. Purcell, P. Vincent, and A. Ayari. Digital and FM Demodulation of a Doubly Clamped Single-Walled Carbon-Nanotube Oscillator: Towards a Nanotube Cell Phone. *Small*, 6(9):1060–1065, 2010.

[38] A. Eichler, J. Moser, J. Chaste, M. Zdrojek, I. Wilson-Rae, and A. Bachtold. Nonlinear damping in mechanical resonators made from carbon nanotubes and graphene. *Nat. Nanotechnol.*, 6(6):339–342, June 2011.

[39] A. K. Huttel, G. A. Steele, B. Witkamp, M. Poot, L. P. Kouwenhoven, and H. S. J. V. D. Zant. Carbon Nanotubes as Ultrahigh Quality Factor Mechanical Resonators. *Nano Lett.*, 9(7):2547–2552, 2009.

[40] B.-R. Choi, A. Hansen, T. Kontos, C. Hoffmann, S. Oberholzer, W. Belzig, C. Schönenberger, T. Akazaki, and H. Takayanagi. Shot-noise and conductance measurements of transparent superconductor/two-dimensional electron gas junctions. *Phys. Rev. B*, 72(2):024501, July 2005.

[41] Y. Zhang, J. Moser, A. Bachtold, and M. I. Dykman. Interplay of driving and frequency noise in the spectra of vibrational systems. pages 1–10, 2014.

[42] H. B. Meerwaldt, S. R. Johnston, H. S. J. van der Zant, and G. a. Steele. Submicrosecond-timescale readout of carbon nanotube mechanical motion. *Appl. Phys. Lett.*, 103(5):053121, 2013.

[43] K. L. Ekinci, Y. T. Tang, and M. L. Roukes. Ultimate limits to inertial mass sensing based upon nanoelectromechanical systems. *J. Appl. Phys.*, 95(5):2682, March 2004.

[44] H. B. Meerwaldt, G. Labadze, B. H. Schneider, A. Taspinar, Y. M. Blanter, H. S. J. van der Zant, and G. A. Steele. Probing the charge of a quantum dot with a nanomechanical resonator. *Phys. Rev. B*, 86(11):115454, September 2012.

[45] A. N. Cleland and M. L. Roukes. Noise processes in nanomechanical resonators. *J. Appl. Phys.*, 92(5):2758, September 2002.

[46] M. Ganzhorn. *Coupling Magnetism and Mechanics at a molecular scale*. Phd, Universite de Gernoble, 2012.

[47] S. Franssila. *Introduction to Micro Fabrication*. Wiley, 2004.

[48] V. Ngoc-Nguyen. *Synthesis and electronic transport of ultraclean single wall carbon nanotubes*. Phd, Institut Neel, 2012.

[49] Z. Yu, S. Li, and P. Burke. Synthesis of aligned arrays of millimeter long, straight single-walled carbon nanotubes. *Chem. Mater.*, 4(14):3414–3416, 2004.

[50] S. Huang, M. Woodson, R. Smalley, and J. Liu. Growth mechanism of oriented long single walled carbon nanotubes using fast-heating chemical vapor deposition process. *Nano Lett.*, 2004.

[51] A. Reina, M. Hofmann, D. Zhu, and J. Kong. Growth Mechanism of Long and Horizontally Aligned Carbon Nanotubes by Chemical Vapor Deposition. *J. Phys. Chem. C*, 3(111):7292–7297, 2007.

[52] C. P. Deck and K. Vecchio. Prediction of carbon nanotube growth success by the analysis of carboncatalyst binary phase diagrams. *Carbon N. Y.*, 44(2):267–275, February 2006.

[53] M. Kumar and Y. Ando. Chemical Vapor Deposition of Carbon Nanotubes: A Review on Growth Mechanism and Mass Production. *J. Nanosci. Nanotechnol.*, 10(6):3739–3758, June 2010.

[54] A. M. Cassell, J. A. Raymakers, J. Kong, and H. Dai. Large Scale CVD Synthesis of Single-Walled Carbon Nanotubes. *J. Phys. Chem. B*, 103(31):6484–6492, August 1999.

[55] N. R. Franklin, Y. Li, R. J. Chen, A. Javey, and H. Dai. Patterned growth of single-walled carbon nanotubes on full 4-inch wafers. *Appl. Phys. Lett.*, 79(27):4571–4573, December 2001.

[56] M. S. Dresselhaus, A. Jorio, A. G. Souza Filho, and R. Saito. Defect characterization in graphene and carbon nanotubes using Raman spectroscopy. *Philos. Trans. A. Math. Phys. Eng. Sci.*, 368(1932):5355–77, December 2010.

[57] A. Ferrari and J. Robertson. Resonant Raman spectroscopy of disordered, amorphous, and diamondlike carbon. *Phys. Rev. B*, 64(7):075414, July 2001.

[58] C. Hierold. *Carbon Nanotube Devices*. Wiley-VCH Verlag GMBH Co., 2008.

[59] C. M. Aguirre, P. L. Levesque, M. Paillet, F. Lapointe, B. C. St-Antoine, P. Desjardins, and R. Martel. The Role of the Oxygen/Water Redox Couple in Suppressing Electron Conduction in Field-Effect Transistors. *Adv. Mater.*, 21(30):3087–3091, August 2009.

[60] M. Ganzhorn and W. Wernsdorfer. Dynamics and Dissipation Induced by Single-Electron Tunneling in Carbon Nanotube Nanoelectromechanical Systems. *Phys. Rev. Lett.*, 108(17):175502, April 2012.

[61] H. O. H. Churchill. *Quantum Dots in Gated Nanowires and Nanotubes*. Phd, Harvard University, May 2012.

[62] B. Gao, E. A. Osorio, K. Babaei Gaven, and H. S. J. van der Zant. Three-terminal electric transport measurements on gold nano-particles combined with ex situ TEM inspection. *Nanotechnology*, 20(41):415207, October 2009.

[63] A. Danilov, D. Golubev, and S. Kubatkin. Tunneling through a multigrain system: Deducing sample topology from nonlinear conductance. *Phys. Rev. B*, 65(12):125312, March 2002.

[64] C. W. J. Beenakker. Theory of Coulomb-blockade oscillations in the conductance of a quantum dot. *Phys. Rev. B*, 44:1646, 1991.

[65] W. G. van der Wiel, S. D. Franceschi, J. M. Elzerman, T. Fujisawa, S. Tarucha, and L. P. Kouwenhoven. Electron transport through double quantum dots. *Rev. Mod. Phys.*, 75(January):1–22, 2003.

[66] E. Minot, Y. Yaish, V. Sazonova, J.-Y. Park, M. Brink, and P. McEuen. Tuning Carbon Nanotube Band Gaps with Strain. *Phys. Rev. Lett.*, 90(15):156401, April 2003.

[67] H. W. Postma, T. Teepen, Z. Yao, M. Grifoni, and C. Dekker. Carbon nanotube single-electron transistors at room temperature. *Science*, 293(5527):76–9, July 2001.

[68] P. Stokes and S. I. Khondaker. Controlled fabrication of single electron transistors from single-walled carbon nanotubes. *Appl. Phys. Lett.*, 92(26):262107, 2008.

[69] P. Stokes, M. R. Islam, and S. I. Khondaker. Low temperature electron transport spectroscopy of mechanically templated carbon nanotube single electron transistors. *J. Appl. Phys.*, 114(8):084311, 2013.

[70] J. Nygå rd and D. H. Cobden. Quantum dots in suspended single-wall carbon nanotubes. *Appl. Phys. Lett.*, 79(25):4216–4218, December 2001.

[71] M. Hatzakis, B. J. Canavello, and J. M. Shaw. Single-Step Optical Lift-off Process. *IBM J. Res. Dev.*, 24(4):452–460, 1980.

[72] Y. Li, W. Kim, Y. Zhang, M. Rolandi, D. Wang, and H. Dai. Growth of Single-Walled Carbon Nanotubes from Discrete Catalytic Nanoparticles of Various Sizes. *J. Phys. Chem. B*, 105(46):11424–11431, November 2001.

[73] Y. Li, J. Liu, Y. Wang, and Z. L. Wang. Preparation of monodispersed Fe-Mo nanoparticles as the catalyst for CVD synthesis of carbon nanotubes. *Chem. Mater.*, 13(3):1008–1014, 2001.

[74] H. Choi, W. Kim, D. Wang, and H. Dai. Delivery of catalytic metal species onto surfaces with dendrimer carriers for the synthesis of carbon nanotubes with narrow diameter distribution. *J. Phys. ...*, 106(48):1–5, 2002.

[75] A. Sharma, S. Tripathi, R. Brajpuriya, T. Shripathi, and S. M. Chaudhari. Thickness Dependent Structural, Magnetic and Transport Properties of Nanostructured Cobalt Thin Films. *J. Nanosci. Nanotechnol.*, 7(6):2041–2045, June 2007.

[76] M. J. Aus, C. Cheung, B. Szpunar, U. . A. Erb, and J. Szpunar. Saturation magnetization of porosity-free nanocrystalline cobalt. *J. Mater. Sci. Lett.*, 17(22):1949–1952, 1998.

[77] B. Witkamp, M. Poot, and H. S. J. van der Zant. Bending-mode vibration of a suspended nanotube resonator. *Nano Lett.*, 6(12):2904–8, December 2006.

[78] B. Witkamp. *High-frequency nanotube resonators*. Phd, Technische Universiteit Delft, 2009.

[79] B. Lassagne, D. Ugnati, and M. Respaud. Ultrasensitive Magnetometers Based on Carbon-Nanotube Mechanical Resonators. *Phys. Rev. Lett.*, 107(13):130801, September 2011.

[80] B. Lassagne, Y. Tarakanov, J. Kinaret, D. Garcia-Sanchez, D. Garcia-Sanchez, and A. Bachtold. Coupling mechanics to charge transport in carbon nanotube mechanical resonators. *Science*, 325(5944):1107–10, August 2009.

[81] J. Yang, Y. Wang, Z. Wang, X. Rong, C.-K. Duan, J.-H. Su, and J. Du. Observing Quantum Oscillation of Ground States in Single Molecular Magnet. *Phys. Rev. Lett.*, 108(23):230501, June 2012.

[82] A. Ardavan, O. Rival, J. J. L. Morton, S. J. Blundell, A. M. Tyryshkin, G. A. Timco, and R. E. P. Winpenny. Will Spin-Relaxation Times in Molecular Magnets Permit Quantum Information Processing? *Phys. Rev. Lett.*, 98(5):057201, January 2007.

[83] S. Bahr, K. Petukhov, V. Mosser, and W. Wernsdorfer. Pump-Probe Experiments on the Single-Molecule Magnet Fe_8: Measurement of Excited Level Lifetimes. *Phys. Rev. Lett.*, 99(14):147205, October 2007.

[84] M. Bal, J. R. Friedman, W. Chen, M. T. Tuominen, C. C. Beedle, E. M. Rumberger, and D. N. Hendrickson. Radiation- and phonon-bottleneck–induced tunneling in the Fe_8 single-molecule magnet. *EPL (Europhysics Lett.*, 82(1):17005, April 2008.

[85] S. Takahashi, J. van Tol, C. C. Beedle, D. N. Hendrickson, L.-C. Brunel, and M. S. Sherwin. Coherent Manipulation and Decoherence of S=10 Single-Molecule Magnets. *Phys. Rev. Lett.*, 102(8):087603, February 2009.

[86] R. Engel-Herbert and T. Hesjedal. Calculation of the magnetic stray field of a uniaxial magnetic domain. *J. Appl. Phys.*, 97(7):074504, 2005.